TU Delft

Delft University of Technology

Document Version
Final published version

Licence
CC BY

Citation (APA)
Laguarda, L., Hickel, S., Schrijer, F. F. J., & van Oudheusden, B. W. (2024). Assessment of Reynolds number effects in supersonic turbulent boundary layers. *International Journal of Heat and Fluid Flow*, *105*, Article 109234. https://doi.org/10.1016/j.ijheatfluidflow.2023.109234

Important note
To cite this publication, please use the final published version (if applicable).
Please check the document version above.

Copyright
In case the licence states “Dutch Copyright Act (Article 25fa)”, this publication was made available Green Open Access via the TU Delft Institutional Repository pursuant to Dutch Copyright Act (Article 25fa, the Taverne amendment). This provision does not affect copyright ownership.
Unless copyright is transferred by contract or statute, it remains with the copyright holder.

Sharing and reuse
Other than for strictly personal use, it is not permitted to download, forward or distribute the text or part of it, without the consent of the author(s) and/or copyright holder(s), unless the work is under an open content license such as Creative Commons.

Takedown policy
Please contact us and provide details if you believe this document breaches copyrights.
We will remove access to the work immediately and investigate your claim.

This work is downloaded from Delft University of Technology.

International Journal of Heat and Fluid Flow 105 (2024) 109234

Contents lists available at ScienceDirect

International Journal of Heat and Fluid Flow

journal homepage: www.elsevier.com/locate/ijhff

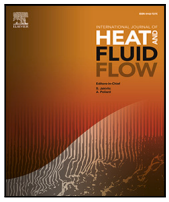

Assessment of Reynolds number effects in supersonic turbulent boundary layers

L. Laguarda *, S. Hickel, F.F.J. Schrijer, B.W. van Oudheusden

Department of Flow Physics and Technology, Faculty of Aerospace Engineering, Delft University of Technology, Kluyverweg 1, Delft, 2629HS, The Netherlands

ARTICLE INFO

Dataset link: https://www.inca-cfd.com

Keywords:
Compressible wall-bounded turbulence
Supersonic boundary layer
Large-eddy simulation

ABSTRACT

Wall-resolved large-eddy simulations (LES) are performed to investigate Reynolds number effects in supersonic turbulent boundary layers (TBLs) at Mach 2.0. The resulting database covers more than a decade of friction Reynolds number Re_τ, from 242 to 5554, which considerably extends the parameter range of current high-fidelity numerical studies. Reynolds number trends are identified on a variety of statistics for skin-friction, velocity and thermodynamic variables. The efficacy of recent scaling laws as well as compressibility effects are also assessed. In particular, we observe the breakdown of Morkovin's hypothesis for third-order velocity statistics, in agreement with previous observations for variable-property flows at low Mach number. Special attention is also placed on the size and topology of the turbulent structures populating the TBL, with an emphasis on the outer-layer motions at high Reynolds number. The corresponding streamwise spectra of streamwise velocity fluctuations show a clear separation between inner and outer scales, where energetic peaks are found at streamwise wavelengths of $\lambda_x^+ \approx 700$ and $\lambda_x/\delta_0 \approx 6$. The spanwise spacing of the outer-layer structures, in turn, is found to be insensitive to the Reynolds number and equal to $\sim 0.7\delta_0$. It is also found that the integral length-scales in spanwise direction for the temperature, streamwise and spanwise velocity fields appear to progressively collapse with increasing Reynolds number. The modulating influence that the outer-layer structures exert on the near-wall turbulence is also clearly visible in many of the metrics discussed. In addition, the present LES data is further exploited to assess the Re_τ-sensitivity of uniform momentum regions in the flow. We find that the resulting probability density function of the number of zones as well as its evolution with Re_τ agrees well with incompressible data. This suggests that uniform zones, which have been associated with outer-layer dynamics, are not strongly influenced by compressibility at the considered Mach number.

1. Introduction

In the compressible regime, turbulent boundary layers (TBLs) are characterized by large mean-property variations, dilatational fluctuations and other phenomena such as localized shocklets (Smits and Dussauge, 2006). These features emerge as a consequence of the strong non-linear coupling between vorticity, entropy and acoustic fields, which increases the complexity of the flow physics compared to the incompressible case.

Statistical models for the description of TBLs were typically first developed for incompressible flows and later adapted to account for compressibility effects. While some of these effects are still under investigation (Yu et al., 2019), many models simply revert to the classic hypothesis by Morkovin (1962) for the treatment of compressible TBL data at relatively low Mach number. Within this paradigm, compressibility effects are approximated with suitable scalings that account for the mean gradients of temperature, density and viscosity in the boundary layer. The validity of this hypothesis has been assessed in multiple works (Duan et al., 2011; Shahab et al., 2011; Wenzel et al., 2018) along with the strong Reynolds analogy (SRA), which further assumes negligible total temperature fluctuations and a perfect anti-correlation between the streamwise velocity and temperature fields (Morkovin, 1962). Even though their applicability has been shown to be questionable (Gaviglio, 1987; Huang et al., 1995; Guarini et al., 2000), these assumptions and related extensions are commonly employed for turbulence modeling due to the lack of better alternatives.

In addition, an important fraction of the available turbulence data has been obtained at relatively low Reynolds numbers. This is specially the case for direct numerical simulations (DNS) of compressible TBL flows, where the Reynolds number dictates the (often prohibitive) grid resolution requirements (Choi and Moin, 2012). The work of Pirozzoli

* Corresponding author.
E-mail address: L.LaguardaSanchez@tudelft.nl (L. Laguarda).

https://doi.org/10.1016/j.ijheatfluidflow.2023.109234
Received 10 February 2023; Received in revised form 5 October 2023; Accepted 17 October 2023
Available online 9 November 2023
0142-727X/© 2023 The Author(s). Published by Elsevier Inc. This is an open access article under the CC BY license (http://creativecommons.org/licenses/by/4.0/).

and Bernardini (2011) constituted the first DNS investigation that considered a compressible TBL at a moderate viscous Reynolds number of $Re_\tau \approx 1100$, where inner and outer scale separation is emerging. By comparing the corresponding results with low-Reynolds simulations, the authors discuss Reynolds number trends on a wide variety of statistics and further highlight the experimentally observed influence of emerging outer-layer structures on the near-wall turbulence. A follow-up work by the same authors included an additional simulation at $Re_\tau \approx 4000$ (Pirozzoli and Bernardini, 2013), where scale separation is much more pronounced. Up to date, this is the highest Reynolds number attained for a supersonic TBL with high-fidelity simulations, which the authors used to complement their previous discussion on Reynold number effects. The analysis of their high-Reynolds data, however, was not as extensive as in the previous study at lower Re_τ. More recently, DNS data at $Re_\tau \approx 1200$ and $Re_\tau \approx 2000$ has also been reported by Huang et al. (2022) and Cogo et al. (2022) for TBLs at both supersonic and hypersonic conditions, where the effects of Mach number and strong wall-cooling were also explored.

Clearly, the amount of high-fidelity numerical datasets is nowadays still very limited, which calls for additional studies in the moderately-high Reynolds number regime. While the current parameter range for compressible TBLs can be more easily expanded with experimental investigations (Ganapathisubramani et al., 2006; Elsinga et al., 2010; Bross et al., 2021), these alone cannot provide full non-intrusive access to all flow variables and regions of interest. For high-fidelity model development, complementary numerical investigations need to fill in the gaps. This constitutes a unique opportunity for large-eddy simulations (LES), where a time-accurate prediction of the unsteady flow is obtained at a reduced computational costs compared to DNS (Choi and Moin, 2012). In conventional LES, only the integral scales are resolved by the computational grid and the effect of the unresolved subgrid-scales (SGS) is accounted for with a SGS model. This implies a compromise between accuracy and computational costs; however, under-resolving (and therefore completely modeling) the near-wall structures would put into question the reliability of the resulting dataset for fundamental research. Considering the relevance of the near-wall turbulence cycle and the fact that this region is often inaccessible in experiments, a much more significant approach is to perform wall-resolved LES of the TBL flow. In this case, the local grid resolution close to the wall is typical of DNS rather than conventional LES. While being computationally more expensive, wall-resolved LES is still less demanding than full DNS and the quality of the resulting data, if conducted properly, is essentially the same (Schlatter et al., 2010).

In this study, we therefore perform wall-resolved LES of compressible TBLs at Mach 2.0 to address the need for additional data as well as to investigate and characterize Reynolds number effects. The resulting database covers more than a decade of Re_τ, from 242 to 5554, which considerably extends the parameter range of current high-fidelity numerical studies. Reynolds number trends are identified on a variety of statistics for skin-friction, velocity, and thermodynamic variables. We further assess the efficacy of recent scaling laws and compressibility effects in the parameter range considered. Particular attention is also placed on the turbulent structures that populate the TBL, with an emphasis on the outer-layer motions at high Reynolds number, which are accurately characterized. In addition, we use the database to investigate uniform momentum regions in the flow (Adrian et al., 2000). For incompressible wall-bounded turbulence, the average number of uniform regions exhibits a characteristic Reynolds number dependency that could be linked to the meandering motions of the outer-layer structures (de Silva et al., 2016; Laskari et al., 2018). Since no such study is available in literature for compressible wall-bounded turbulence, the present LES data is exploited to characterize for the first time the Re_τ-sensitivity of uniform regions in supersonic TBLs. Finally, the distribution of thermodynamic fluctuations as well as their mutual interaction with the velocity field is also analyzed in detail, since these play important roles in compressible turbulence.

Table 1
Details of the present simulations.

Case	Re_τ	Re_θ	Re_{δ_0} [$\times 10^{-3}$]	$\Delta x^+_{min} \times \Delta y^+_{min} \times \Delta z^+_{min}$	Legend
$\mathcal{T}_1$	242–402	1093–1786	12.1–19.6	$21.8 \times 0.93 \times 7.7$	– – –
$\mathcal{T}_2$	949–1338	4167–6381	50.2–74.1	$39.0 \times 0.94 \times 9.8$	–·–·–
$\mathcal{T}_3$	3897–5554	20 846–28 892	243.4–360.3	$38.5 \times 0.94 \times 10.2$	——

The paper is structured as follows. In Section 2 we briefly describe the numerical methodology as well as the investigated flow cases. Simulation results are then presented and discussed in Section 3: Section 3.1 focuses on mean and fluctuating skin-friction distributions, Section 3.2 discusses velocity statistics, Section 3.3 introduces different statistical properties of turbulent structures, and Section 3.4 includes the analysis of thermodynamic fluctuations and related quantities. The paper is finally concluded in Section 4 along with further remarks.

2. Numerical methodology

We present wall-resolved LES data for spatially developing zero-pressure-gradient turbulent boundary layers at Mach 2.0 and different Reynolds numbers, from $Re_\tau \approx 250$ to $Re_\tau \approx 5550$. The database comprises three independent simulations, $\mathcal{T}_1$, $\mathcal{T}_2$ and $\mathcal{T}_3$, for which the range of Reynolds number from inflow to outflow plane is provided in Table 1. As observed, the present study covers more than a decade of Re_τ which allows for a detailed characterization of Reynolds number effects. The line legend is also included in Table 1 for later reference.

In all cases, the stagnation temperature and pressure are set to $T_0 = 288$ K and $p_0 = 356$ kPa respectively, and the free-stream flow velocity is $u_\infty = 507$ m/s. At the inflow plane, the 99% velocity-based boundary layer thickness $\delta_{0,in}$ is 5.2 mm. The considered fluid is air with a specific heat capacity ratio of $\gamma = 1.4$, a specific gas constant of $\mathcal{R} = 287.05$ J(kg K)$^{-1}$ and a molecular Prandtl number of $Pr = 0.72$. The temperature dependency of the dynamic viscosity is modeled through Sutherland's law and the heat flux is modeled by Fourier's law with a thermal conductivity proportional to the dynamic viscosity.

The computational domain is rectangular with dimensions $[L_x, L_y, L_z] = [45.5, 16.5, 4]\delta_{0,in}$. Details about the grid spacing in viscous units are also provided in Table 1. Note that the spatial resolution at the wall is sufficiently large in all cases to properly resolve the wall shear stress $\tau_w = \mu_w \partial u/\partial y|_w$ and the dynamically relevant turbulent structures. Away from the wall plane, a block-wise coarsening is applied in streamwise and spanwise direction as shown in Fig. 1 for the computational domain of the high-Reynolds case $\mathcal{T}_3$. Only one direction is coarsened from one row of blocks to the one above, and always with an expansion ratio of 2. In addition, a grid stretching with constant stretching factor is applied in wall-normal direction. Fig. 1 also indicates the origin of coordinates, which is placed at the inflow plane, on the wall and half way between the spanwise boundaries.

A non-reflecting boundary condition based on Riemann invariants is used at the top and outflow boundaries of the computational domain (Poinsot and Lele, 1992), and periodicity is imposed in the spanwise direction. The wall is modeled as isothermal at the free-stream stagnation temperature, i.e., $T_w = T_0$. Based on the nominal adiabatic wall-temperature, i.e., $T_{aw} = T_\infty[1 + r(\gamma - 1)M^2_\infty/2]$ with a recovery factor $r = Pr^{1/3}$, the ratio of wall-temperature to adiabatic wall-temperature is $T_w/T_{aw} = 1.05$. Furthermore, the digital filter technique of Xie and Castro (2008) is used at the inflow plane to prescribe adequate turbulent boundary conditions with well-defined space and time correlations. Details about the implementation of the filtering procedure are provided in Laguarda and Hickel (2023) and the employed digital filter settings in the present simulations correspond to those for case $A2$ in their publication. These include a correlation function for tangential directions of the form

$$R(r) = (1 - r/I)\ \exp\ (-r/I) \tag{1}$$

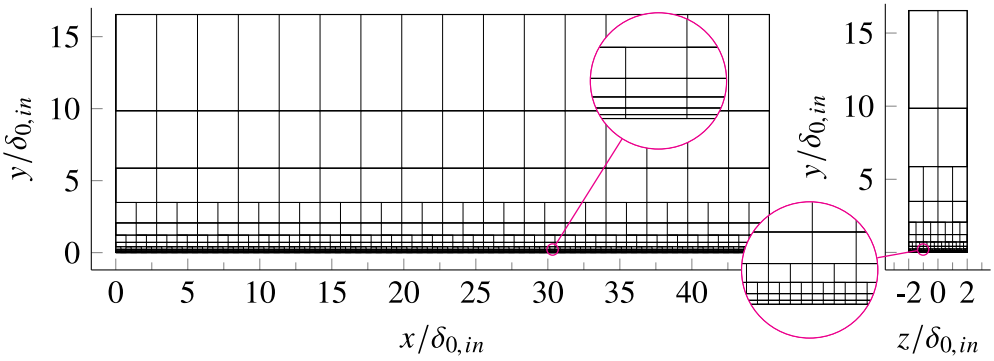

Fig. 1. Block distribution of the numerical grid for the high-Reynolds case $\mathcal{T}_3$.

Table 2
Target length scales per velocity component, spatial direction and considered zone.
Source: Laguarda and Hickel (2023).

Zone	Range	L_{ref}	I_x/L_{ref}			I_y/L_{ref}			I_z/L_{ref}		
			u	v	w	u	v	w	u	v	w
1	0 to $y^+ = 100$	l^+_{in}	400	100	60	75	100	50	100	50	100
2	$y^+ = 100$ to $0.2\delta_{0,in}$	$\delta_{0,in}$	1.2	0.2	0.3	0.2	0.2	0.15	0.2	0.15	0.3
3	Above $0.2\delta_{0,in}$	$\delta_{0,in}$	0.9	0.3	0.3	0.3	0.3	0.25	0.35	0.25	0.35

where I is the target length scale. This form allows for negative correlation values near $r = 0$ which is in better agreement with tangential correlation functions measured in DNS studies of wall-bounded turbulence (Pirozzoli and Bernardini, 2011). Additionally, three zones with different target length scales are specified at the inflow plane to realistically account for the variation of the TBL structure with wall-distance (Veloudis et al., 2007; Laguarda and Hickel, 2023). The employed scales are specified in Table 2 per velocity component, spatial direction and considered zone. Note that only zones 1 and 3 were used in the low-Reynolds case $\mathcal{T}_1$ due to the absence of a fully established quasi-logarithmic layer. The prescribed first and second-order statistical moments at the inflow plane are derived from the DNS database of Pirozzoli and Bernardini (2011, 2013) for supersonic TBLs at Mach 2.0.

All simulations are performed with the finite volume solver INCA (https://www.inca-cfd.com), which employs the adaptive local deconvolution method (ALDM) for LES of the compressible Navier–Stokes equations (Hickel et al., 2014). ALDM is a nonlinear solution-adaptive finite volume method that exploits the discretization of the convective fluxes to introduce a physically consistent sub-grid scale turbulence model. Diffusive fluxes are approximated by second-order schemes and a third-order total variation diminishing Runge–Kutta scheme is employed for time integration. The reader is referred to Hickel et al. (2014) for implementation details of the method and validation results.

Each simulation was carried on as follows. First, an initial transient of 10 flow-through times (FTT) of the full domain length was simulated to ensure a fully developed turbulent flow in statistical equilibrium. This solution interval was discarded from the present analysis. After this transient, simulations were integrated for another 12 FTT of the full domain length. During this second interval, approximately 40 000 statistics samples were collected at a sampling interval of $\Delta t u_\infty/\delta_{0,in} \approx 0.013$ and averaged in the homogeneous spanwise direction and in time. In addition, three-dimensional snapshots of the full domain were stored at regular intervals of $\Delta t u_\infty/\delta_{0,in} \approx 2$, leading to an ensemble of approximately 250 snapshots stored per case.

3. Results and discussion

The resulting LES database is exploited to characterize the effect of Reynolds number on the flow. Unless otherwise stated, profiles are extracted at $x/\delta_{0,in} = 40$, corresponding to $Re_\tau \approx 382$, 1291 and 5371 for the three cases.

3.1. Skin-friction

The evolution of the skin-friction coefficient starting from $x/\delta_{0,in} = 5$ is shown in Fig. 2(*a*). The van Driest II transformation (Van Driest, 1956) is employed to remove Mach number effects and enable comparison with well established correlations for incompressible boundary layers. That is, skin-friction and Reynolds number are reduced to their equivalent incompressible values by means of the following transformation

$$c_{f,i} = F_c c_f, \quad Re_{\theta,i} = \frac{\mu_\infty}{\mu_w} Re_\theta. \tag{2}$$

where F_c is a function of the wall temperature T_w and nominal adiabatic wall temperature T_{aw}, see, e.g., Shahab et al. (2011) or Hadjadj et al. (2015). As observed in Fig. 2(*a*), our LES data agrees very well with the considered correlations. Most notably, the skin-friction distribution for the high-Reynolds case $\mathcal{T}_3$ closely follows the Kármán–Schoenherr correlation (dashed line). This is in agreement with the work of Bross et al. (2021) who experimentally investigated zero-pressure-gradient TBLs over a wide range of Reynolds and Mach numbers and found that the agreement between the corresponding skin-friction distributions and the Kármán–Schoenherr correlation improved with increasing Reynolds number.

The fluctuation magnitude of the wall-shear stress $\tau^+_{w,rms}$ over the second half of the LES domain is shown in Fig. 2(*b*). A value in the range of 0.41 to 0.46 is obtained for the considered TBLs, indicating that the fluctuating component of the wall-shear stress amounts to almost half of the corresponding mean value. Fig. 2(*b*) also reveals a clear $\tau^+_{w,rms}$ dependency on the Reynolds number, with fluctuation magnitudes increasing with Re_τ. The resulting trend closely follows the linear relation of Schlatter and Örlü (2010) derived from incompressible data (dash-dotted line), which confirms the fully developed state of the near-wall turbulence in all cases.

3.2. Velocity statistics

In line with previous works at moderate Mach numbers (Pirozzoli and Bernardini, 2011; Lagha et al., 2011b), the maximum magnitude of the fluctuating Mach number measured is $\sqrt{M'^2} \approx 0.2$. Therefore, genuine compressibility effects are typically expected to be small (Smits and Dussauge, 2006) and the Morkovin's hypothesis to hold. That is, deviations from incompressible data are mainly associated with

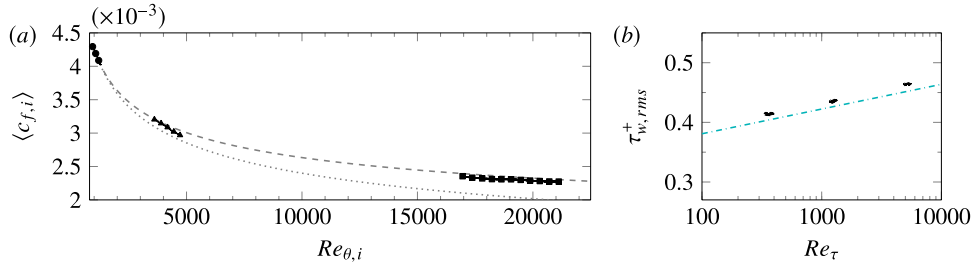

Fig. 2. Incompressible skin-friction distributions for case $\mathcal{T}_1$ (●), case $\mathcal{T}_2$ (▲) and case $\mathcal{T}_3$ (■). Dashed and dotted lines respectively denote the incompressible correlation of Kármán–Schoenherr (Schoenherr, 1932; Hopkins and Inouye, 1971) and $c_{f,i} = 0.024 Re_{\theta,i}^{-1/4}$ (Smits et al., 1983).

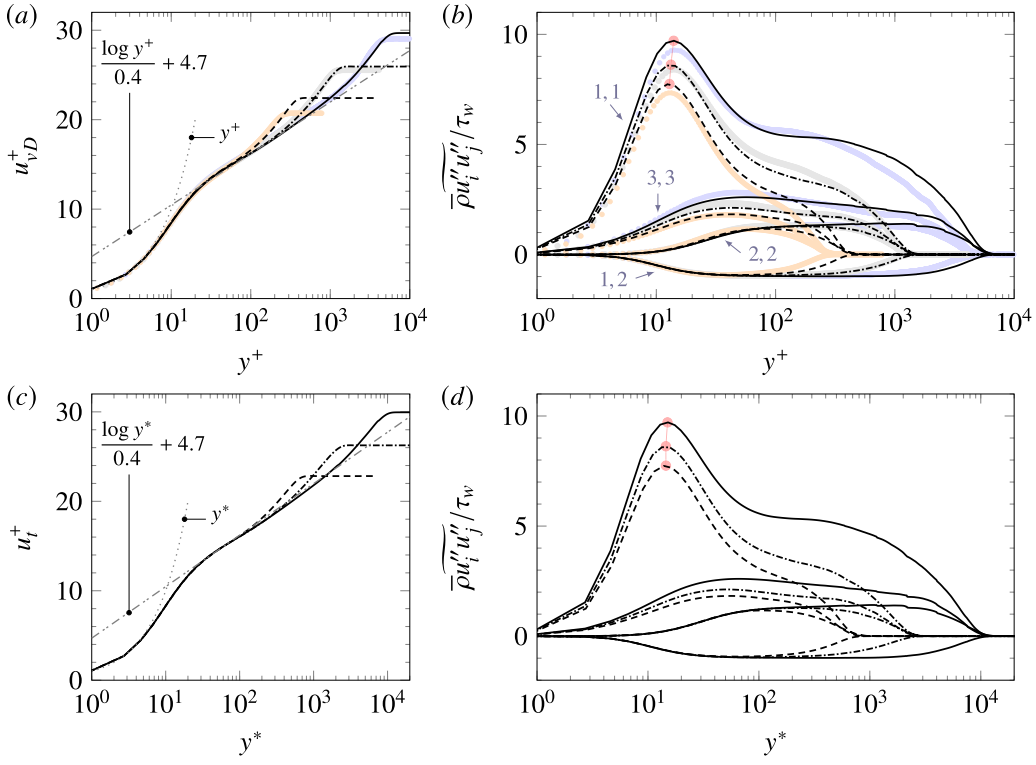

Fig. 3. First and second-order velocity statistics: (a) – (b) van Driest transformed mean velocity and density-scaled Reynolds stresses over the inner-scaled wall-distance y^+, and (c) – (d) total-stress-based transformed mean velocity and density-scaled Reynolds stresses over the semi-local wall-distance y^* (see Eqs. (3) and (4)). For reference, DNS data of Pirozzoli and Bernardini (2011, 2013) at Mach 2.0 and $Re_\tau \approx [250, 1100, 4000]$ is respectively indicated in panels (a) and (b) with orange, gray and blue markings. The indices i, j for the Reynolds stresses are indicated in panel (b), while red circles in both panels (b) and (d) highlight the peak value of the streamwise stress. (For interpretation of the references to color in this figure legend, the reader is referred to the web version of this article.)

the variation of mean thermodynamic quantities across the boundary layer (rather than their fluctuations) and do not fundamentally alter turbulence characteristics (Morkovin, 1962). Under this assumption, incompressible velocity statistics should be recovered by simply accounting for mean-property variations.

Fig. 3(a) shows the van Driest-transformed mean velocity profile u^+_{vD} for each case, where $du^+_{vD} = \sqrt{\overline{\rho}/\overline{\rho}_w} d\widetilde{u}^+$ accounts for mean density variations. As observed, the transformed profiles exhibit the typical incompressible behavior, with a near-wall viscous sub-layer (where linear scaling $u^+_{vD} = y^+$ holds until $y^+ \approx 5$) and a quasi-logarithmic layer (with close $u^+_{vD} = (1/\kappa)\log y^+ + C$ behavior). The latter is not fully established for case $\mathcal{T}_1$, which is expected at low Reynolds number. For case $\mathcal{T}_3$, on the other hand, the quasi-logarithmic layer extends for more than a decade of inner-scaled wall-distance, from $y^+ \approx 40$ until $y^+ \approx 700$, and conforms to a log-law with a von Kármán constant of $\kappa = 0.4$ and an intercept value of $C = 4.7$. Despite the visually well established logarithmic behavior, however, the diagnostic function $\Xi = y^+ du^+_{vD}/dy^+$ for this case (not shown here) is not constant but rather increases in this region, crossing the theoretical $1/\kappa$ value required for pure logarithmic behavior. As for the wake region, we measure a wake parameter of $\Pi = 0.48$ for case $\mathcal{T}_1$, $\Pi = 0.58$ for case $\mathcal{T}_2$ and $\Pi = 0.63$ for case $\mathcal{T}_3$. These values are consistent with the expected wake parameter dependence on the momentum-thickness Reynolds number and agree well with previous simulations of compressible TBLs (Gatski and Bonnet, 2013).

Density-scaled Reynolds stresses are reported in Fig. 3(b) and exemplary illustrate Reynolds number effects in the TBL topology. Most notably, the viscous-scaled fluctuation intensity for the wall-parallel components increases with Re_τ. This is a direct effect of the emergent large-scale coherent motions in the near-logarithmic region, whose contributions to the wall-parallel velocity variances is increasingly significant with Reynolds number (Hutchins and Marusic, 2007a). The observed increase in streamwise stress near the wall also reveals the modulating influence that such outer-layer motions have on the near-wall cycle (Hutchins and Marusic, 2007b). Despite the fact that the viscous-scaled near-wall turbulence is a self-sustaining process (Jiménez and Pinelli, 1999; Lagha et al., 2011a), large-scale variations in the velocity fluctuations away from the wall are known to modulate near-wall

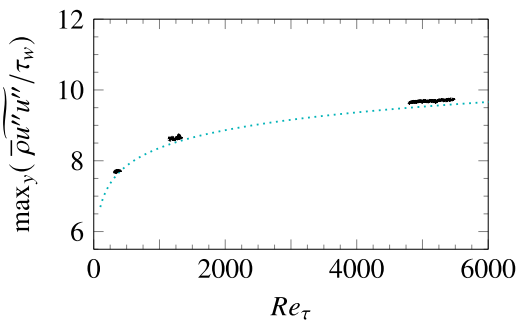

Fig. 4. Distribution of the peak value for the density-scaled streamwise Reynolds stress. Line style legend: (——) present LES data, (·····) logarithmic fit to the DNS data of Pirozzoli and Bernardini (2011, 2013) at Mach 2.0.

fluctuations (Hutchins and Marusic, 2007b) which overall increase with Reynolds number (Hoyas and Jiménez, 2006). The formation of a distinct plateau for the shear stress, which is clearly visible for case $\mathcal{T}_3$ in Fig. 3(*b*), is also a direct Reynolds number effect. This plateau corresponds to the formation of a quasi-equilibrium layer where production of turbulence kinetic energy approximately balances dissipation (Townsend, 1961). Other visible Reynolds number effects on the velocity variances concern the wall-normal component, whereby its peak location moves from the inner part to the outer part of the boundary layer at sufficiently high Re_τ.

For reference purposes, DNS data of Pirozzoli and Bernardini (2011, 2013) for supersonic TBLs at Mach 2.0 and various Reynolds numbers is also included in Fig. 3(*a*) and (*b*) (indicated with markers). Overall, the present LES data agrees very well with the DNS data, with minor differences attributed to different friction Reynolds numbers (particularly visible at the boundary layer edge). We also note that the peak value for the streamwise stress is very well captured in the present simulations, and closely follows the logarithmic fit to the reference DNS data (Pirozzoli and Bernardini, 2013), see Fig. 4.

We recall that the wall-temperature in the present simulations is very close to its nominal adiabatic value, i.e., $T_w/T_{aw} = 1.05$. However, the employed wall condition is strictly non-adiabatic, and the accuracy of the van Driest transformation is known to deteriorate with (increasing) non-adiabatic conditions (Trettel and Larsson, 2016; Huang et al., 2022). Therefore, alternative transformations to that of van Driest are also considered here to assess whether the collapse of the mean velocity profiles can improve to any extent. Particularly, we consider the transformation proposed by Trettel and Larsson (2016), which is identical to that of Patel et al. (2015), as well as the transformation proposed by Griffin et al. (2021). The former is grounded on the premise that a transformed logarithmic law shall preserve the momentum balance in the transformed state. This gives rise to a transformation kernel for both the mean velocity profile as well as the wall-distance coordinate, the later coinciding with the semi-local scaling $y^* = y/l^*$ of Huang et al. (1995), where

$$l^* = l^+ \frac{\overline{\mu}}{\mu_w}\sqrt{\frac{\rho_w}{\overline{\rho}}}, \tag{3}$$

is the semi-local viscous length scale (Trettel and Larsson, 2016). We also note that the earlier work of Patel et al. (2015) provides a different foundation for the applicability of the same transformation. By re-scaling the Navier–Stokes equations with local quantities, the authors demonstrate that the van Driest transformed velocity as well as second-order turbulent statistics depend on the semi-local viscous Reynolds number $Re_\tau = \delta/l^*$.

The transformation proposed by Patel et al. (2015) and Trettel and Larsson (2016) was tested on the present LES data and led to an increased scatter along the buffer and quasi-logarithmic layers. Other authors have reported similar effects (Griffin et al., 2021; Huang et al., 2022; Cogo et al., 2022) and for the sake of brevity, the resulting transformed profiles are not shown here. As indicated by Griffin et al. (2021), the increased scatter is attributed to the over-prediction of the mean shear in the beginning of the logarithmic layer, which directly stems from the resulting viscous stress invariance of this transformation throughout the whole boundary layer (instead of only within the viscous sub-layer). In view of this issue, Griffin et al. (2021) proposed a modified transformation that treats viscous and Reynolds stresses independently and only in their respective domains of applicability. That is, the semi-local scaling proposed by Patel et al. (2015) and Trettel and Larsson (2016) is recovered for the viscous stresses near the wall while the Reynolds shear stress away from the wall is scaled assuming an approximate balance between turbulence production and dissipation (Griffin et al., 2021). The resulting transformation is referred to as the total-stress-based transformation $u_t[y^*] = \int S_t^+ dy^*$, where

$$S_t^+ \approx \frac{S_{eq}^+}{1 + S_{eq}^+ + S_v^+}, \tag{4}$$

and $S_{eq}^+ = (\mu_w/\overline{\mu})(\partial u^+/\partial y^*)$ and $S_v^+ = (\overline{\mu}/\mu_w)(\partial u^+/\partial y^+)$.

Careful inspection of the total-stress-based transformed mean velocity profiles against the semi-local wall-distance coordinate y^*, which are shown in Fig. 3(*c*), reveals some improvements in the data collapse along the linear and particularly the buffer layer compared to the van Driest transformed profiles of Fig. 3(*a*). Additionally, it does not increase the scatter in the quasi-logarithmic layer, overcoming the shortcomings of the transformation proposed by Patel et al. (2015) and Trettel and Larsson (2016). This shows the enhanced capabilities of the total-stress-based scaling, even for TBLs with quasi-adiabatic wall conditions. As for the boundary layer wake, the data scatter still remains albeit with a slightly reduced deviation from the quasi-logarithmic behavior compared to Fig. 3(*a*).

Regarding second-order statistics, Patel et al. (2015) argue that data for variable property flows should also reduce to their constant property counterparts by simply employing the semi-local inner coordinate y^*. In order to assess the validity of this scaling for the Reynolds stresses, they are shown in 3(*d*) against y^*. Overall, improvements in the data collapse are not apparent when compared to Fig. 3(*b*). However, the semi-local scaling does improve the overlap of the wall-normal stress profiles in the linear and buffer layer, and leads to a better alignment of the near-wall streamwise stress peak (indicated with red circles).

The effect of Reynolds number on the streamwise velocity statistics is now assessed by inspecting the corresponding skewness $S(u) = \overline{u'^3}/\overline{u'^2}^{3/2}$ and flatness $F(u) = \overline{u'^4}/\overline{u'^2}^2$. These distributions are respectively shown in Fig. 5(*a*) and (*b*) where clear differences can be observed. Most notably, both skewness and flatness increase near the wall at high Reynolds number. This could be attributed to the stronger footprint of the log-layer structures on the near-wall turbulence, which becomes more intermittent. The skewness profiles exhibit a qualitatively similar behavior, that is, positive values very close to the wall and a relaxation towards a nearly Gaussian behavior ($S(u) \approx 0$) above the viscous sub-layer. However, $S(u)$ is clearly negative for case $\mathcal{T}_1$ beyond $y^+ \approx 10$, while the profile for the high-Reynolds case $\mathcal{T}_3$ is much closer to zero, i.e., closer to a purely Gaussian behavior. This could be attributed to the presence of a well-established quasi-logarithmic layer in the latter case. The corresponding flatness distributions in this region approach a value of 3 in all cases, see Fig. 5(*b*), which confirms the nearly Gaussian behavior observed in the skewness profiles. However, $F(u)$ also exhibits an apparent Reynolds number dependency beyond $y^+ \approx 30$, since increasingly lower values than 3 are observed at higher Reynolds number. This implies that the tailedness of the corresponding probability distribution decreases with increasing Reynolds number. Moreover, all cases exhibit very similar intermittent behavior towards the edge of the boundary layer, i.e., negative skewness and large flatness, which is caused by outward excursions of low-speed flow

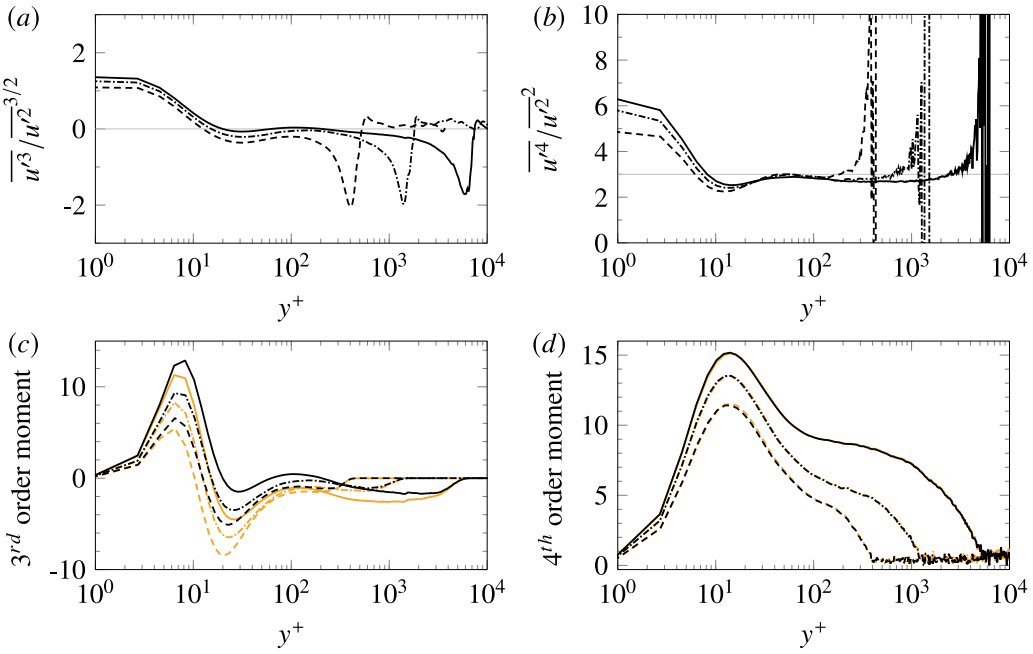

Fig. 5. Higher-order moments of the streamwise velocity: (*a*) skewness, (*b*) flatness, (*c*) density-scaled third-order central moment $\overline{\rho}^{3/2}\overline{u_i'^3}/\tau_w^{3/2}$ (black) and $\overline{\rho}^{3/2}\overline{u_i''^3}/\tau_w^{3/2}$ (orange), and (*d*) density-scaled fourth-order central moment $\overline{\rho}\sqrt{\overline{u_i'^4}}/\tau_w$ (black) and $\overline{\rho}\sqrt{\overline{u_i''^4}}/\tau_w$ (orange). (For interpretation of the references to color in this figure legend, the reader is referred to the web version of this article.)

into the free-stream. Wall-normal distributions of the intermittency coefficient, defined as the fraction of time that the flow is turbulent, were also computed for the investigated TBLs (not shown here) and do not exhibit any apparent Reynolds number dependency.

Before concluding this section, the influence of density fluctuations, and therefore the validity of Morkovin's hypothesis, on high-order statistics is assessed. As already mentioned, Morkovin's hypothesis implies that any statistical moment is independent of the averaging procedure, i.e., Reynolds or Favré averaging. If that is the case, the following relation would hold for the third-order central moment of a velocity component (Patel et al., 2015)

$$\overline{\rho}^{3/2}\overline{u_i'^3}/\tau_w^{3/2} \stackrel{?}{=} \overline{\rho}^{3/2}\overline{u_i''^3}/\tau_w^{3/2}. \tag{5}$$

A single prime denotes a fluctuation from the Reynolds-averaged mean (indicated with an over-bar), while a double prime is used for fluctuations from Favré-averaged quantities. A similar relation would also apply for the fourth-order central moment, i.e.,

$$\overline{\rho}\sqrt{\overline{u_i'^4}}/\tau_w \stackrel{?}{=} \overline{\rho}\sqrt{\overline{u_i''^4}}/\tau_w. \tag{6}$$

In order to assess whether these relations indeed hold, both averaging procedures are compared in Fig. 5(*c*) and (*d*) for the third-order and fourth-order central moments of the streamwise velocity, respectively. As observed, a clear disagreement is found for the third-order moment, see Fig. 5(*c*), where the Reynolds-averaged (black) and Favré-averaged (orange) profiles do not collapse for the cases considered. Patel et al. (2015) reported a similar disagreement for their DNS data of variable-property turbulent channel flows at low Mach number. Our simulations confirm that Morkovin's hypothesis does not hold for third-order statistics of wall-bounded turbulence also in the compressible flow regime. In terms of the fourth-order central moments, see Fig. 5(*d*), good collapse is found between the Reynolds and Favré averaged profiles in all cases, also in agreement with the findings of Patel et al. (2015). Note that this also applies for the other velocity components, but for the sake of brevity the corresponding statistical moments are not included in this paper.

3.3. Turbulence structure

The effect of Reynolds numbers on the statistical properties of turbulent structures is analyzed next. As a starting point, we consider the pre-multiplied streamwise energy spectra of streamwise velocity fluctuations, which are shown in Fig. 6. Only the last third of the LES domain has been considered for the spectra, which have been calculated at selected wall-normal locations that coincide with the computational grid (no interpolation used) and appear approximately equispaced in logarithmic scale. The spectra have been estimated using Welch's algorithm with Hamming windows and 3 segments with 75% overlap, in addition to the averaging in spanwise direction and in time.

As observed, all spectral distributions bear clear similarities very close to the wall, where a peak corresponding to the signature of energetic near-wall streaks is found at $y^+ \approx 15$ in all cases. The wavelength associated with these high- and low-speed regions is approximately constant in viscous units and equal to $\lambda_x^+ \approx 700$, which is in good agreement with previous studies (Hutchins and Marusic, 2007b; Huang et al., 2022). Further away from the wall, however, Fig. 6(*c*) reveals the emergence of energy at high wavelengths for the high-Reynolds case $\mathcal{T}_3$ that is absent in the spectrum for the other cases. This energy increase is already noticeable close to the wall and reaches a local maximum in the quasi-logarithmic region, at about $y/\delta_0 \approx 0.1$. The wavelength associated with this local peak is about $\lambda_x/\delta_0 \approx 6$, which is much larger than the one associated to the near-wall streaks. Clearly, this outer peak is the signature of the emergent large-scale motions in this region. Such bimodal configuration of the streamwise spectra in Fig. 6(*c*), with two competing energetic peaks at different wavelengths, evidences inner/outer scale separation and the genuinely high-Reynolds nature of case $\mathcal{T}_3$ (Hutchins and Marusic, 2007b).

The streamwise–wall-normal organization of the large-scale turbulent structures is further characterized in Fig. 7 by the two-point autocorrelation map of streamwise velocity fluctuations

$$R_{uu}(\Delta x, y) = \frac{\langle u'(x, y, z, t)u'(x + \Delta x, y_{ref}, z, t)\rangle}{\sigma_u(y)\,\sigma_u(y_{ref})}, \tag{7}$$

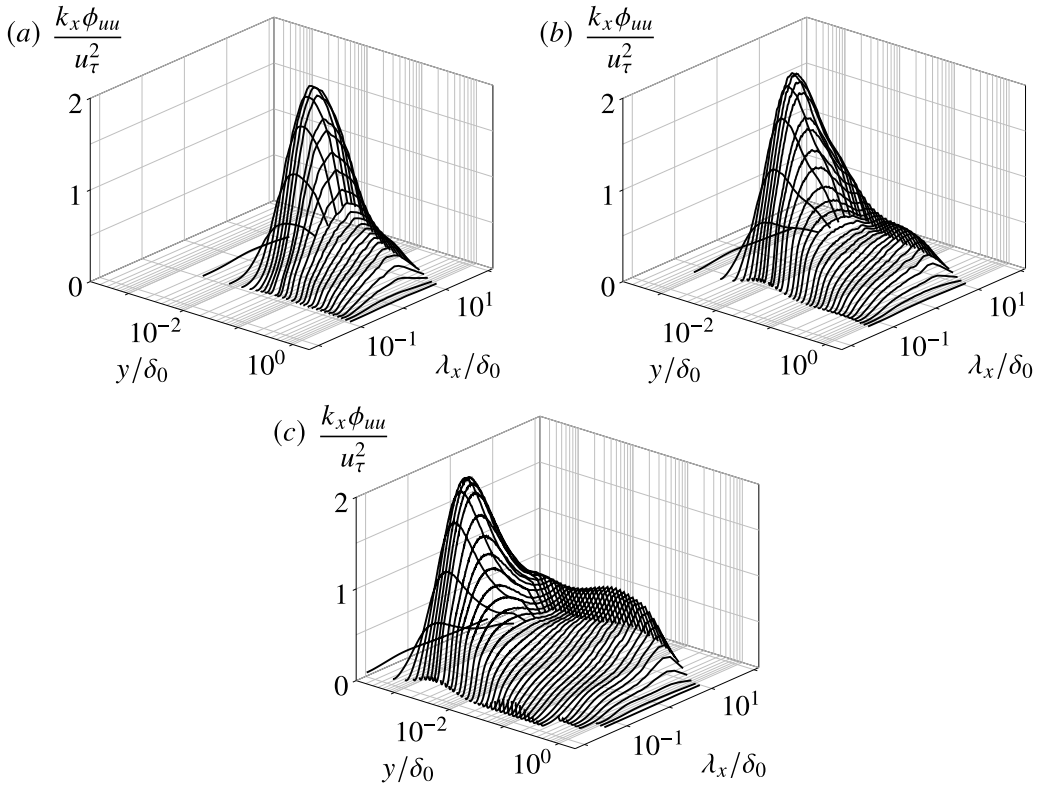

Fig. 6. Streamwise spectra of streamwise velocity fluctuations for (*a*) case $\mathcal{T}_1$, (*b*) case $\mathcal{T}_2$, and (*c*) case $\mathcal{T}_3$.

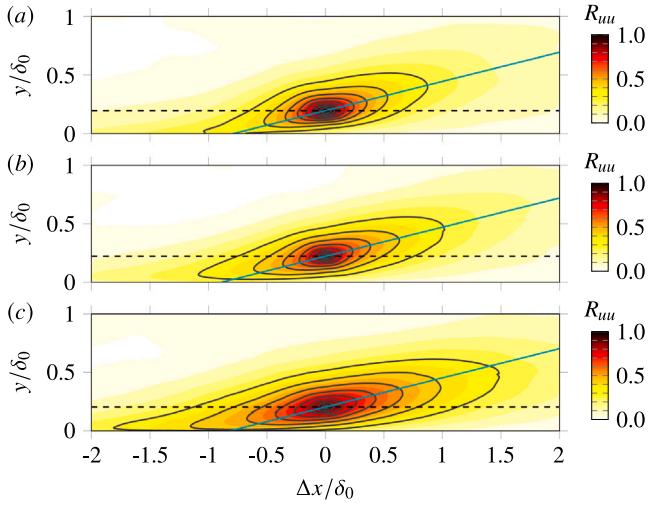

Fig. 7. Two-point autocorrelation map of streamwise velocity fluctuations R_{uu} for (*a*) case $\mathcal{T}_1$, (*b*) case $\mathcal{T}_2$, and (*c*) case $\mathcal{T}_3$. The reference wall-normal location is $y_{ref}/\delta_0 = 0.2$ and the solid black lines indicate contour levels from 0.1 to 0.9 in increments of 0.1. In all figures, a blue line with an inclination of 14° intersecting the maximum correlation point is included for reference. (For interpretation of the references to color in this figure legend, the reader is referred to the web version of this article.)

where the reference wall-normal location y_{ref} is set at $0.2\delta_0$ following Bross et al. (2021). The angle brackets are employed to denote time-, spanwise-, and also streamwise-averaging, over a domain $4\delta_0$ long and centered at $x/\delta_{0,in} = 40$.

The extent of the correlation noticeably increases with increasing Reynolds number, see Fig. 7(*c*), which evidences the corresponding enlargement of the emergent outer-layer motions. The scale interaction between these structures and the near-wall turbulence is also reflected by the increased correlation magnitudes at the wall. This wall-coherence is established at an oblique angle with respect to the free-stream flow, which implies a forward inclination of the log-layer structures. Despite the scatter of the reported inclination angles in literature (Pirozzoli et al., 2008), recent studies reveal a typical eddy orientation between 12° and 20° (Marusic and Heuer, 2007; Ringuette et al., 2008; Pirozzoli and Bernardini, 2011; Bross et al., 2021). The correlation maps in Fig. 7(*a*) and (*b*) for the low- and moderate-Reynolds cases conform well with an inclination of 14° in the outer part of the boundary layer, which corresponds to the value reported by Marusic and Heuer (2007) over a wide range of Reynolds numbers. This inclination is indicated in the figures with a solid blue line. The high-Reynolds case $\mathcal{T}_3$, in turn, exhibits a slightly smaller inclination above y_{ref} of approximately 10°, see Fig. 7(*c*). We also note that all correlation maps conform to more shallow angles between 8° and 11° near the wall (in the region below the reference height). In view of this, a line fit of the peak points in wall-normal direction is considered to be a poor representation of the inclination of the correlation map, and would certainly lead to a smaller inclination angle than 14° in all cases.

The average spanwise spacing of the dominant turbulent structures is assessed from spanwise autocorrelation functions and related spectra to better understand their three-dimensional arrangement. Correlation functions of the velocity components at two different wall-normal locations, i.e., $y^+ \approx 15$ and $y/\delta_0 \approx 0.1$, are shown in Fig. 8. Correlations have been obtained by first applying the Fourier transform to the instantaneous fluctuation distribution in the spanwise direction, then computing the power spectrum and averaging (in Fourier space) over all instances, and finally transforming back to physical space. Note that all variables (also thermodynamic variables, which are not shown) fully de-correlate over a distance smaller than the domain half-width $L_z/2$, see the rights panels of Fig. 8. This confirms that turbulence dynamics in the present simulations do not suffer from limited-span effects.

In all cases, the streamwise velocity correlation calculated at $y^+ \approx 15$ has a local minimum at $\Delta z^+ \approx 50$. This provides an indication of the spanwise spacing between adjacent near-wall streaks, which are characterized by velocity fluctuations of opposite sign. In reference

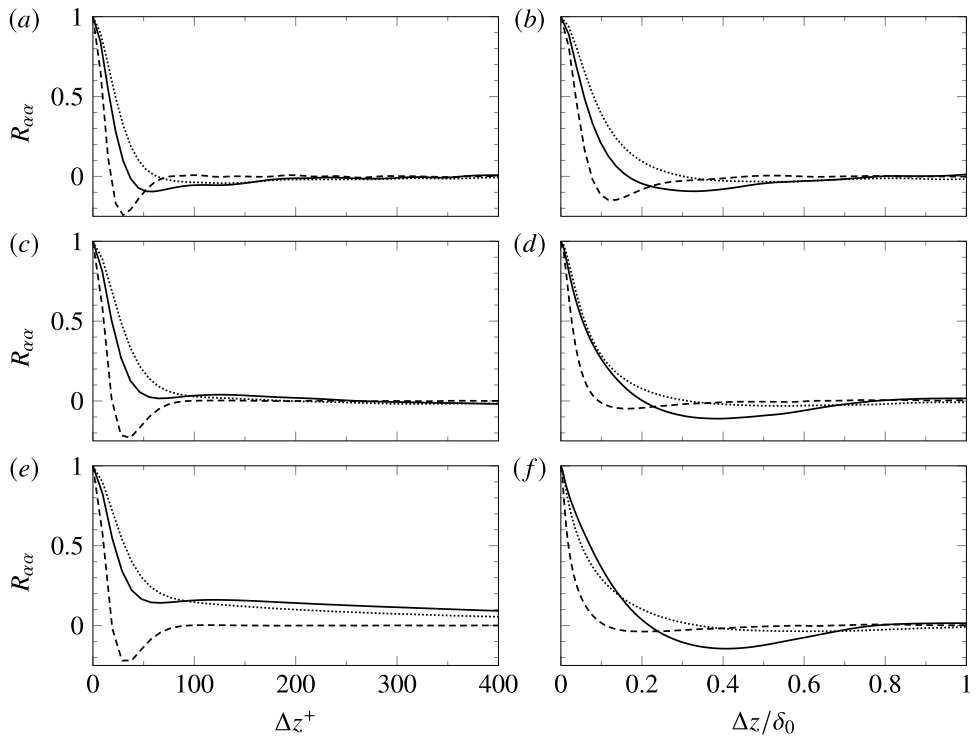

Fig. 8. Two-point autocorrelation functions of the velocity components in the spanwise direction at $y^+ \approx 15$ (left), and $y/\delta_0 \approx 0.1$ (right). Panels (*a*) and (*b*) correspond to case $\mathcal{T}_1$, panels (*c*) and (*d*) to case $\mathcal{T}_2$, and panels (*e*) and (*f*) to case $\mathcal{T}_3$. Line style legend: (——) streamwise velocity, (– – –) wall-normal velocity, (· · · · · ·) spanwise velocity.

investigations of compressible TBLs at lower Reynolds numbers (Pirozzoli et al., 2004; Lagha et al., 2011b), such local minimum is actually global and associated with negative correlation values. As shown in the left panels of Fig. 8, this is true for the low-Reynolds case but no longer holds for the moderate and high-Reynolds TBLs, where the local minimum near the axis is found at $R_{uu} \approx 0$ and $R_{uu} \approx 0.15$ respectively. While the alternating streak pattern of low- and high-momentum regions near the wall is still present in these cases, the increasingly positive value of the local minimum highlights the organizing influence of the emergent outer-layer motions on the small-scale fluctuations near the wall. This influence is better illustrated in Fig. 9 which directly compares the streamwise velocity correlation at $y^+ \approx 15$ with the one obtained at $y/\delta_0 \approx 0.1$. For the high-Reynolds case, see Fig. 9(*b*), the global minimum of the near-wall correlation (black line) clearly coincides with the global minimum of the correlation at $y/\delta_0 \approx 0.1$ (orange line). This further evidences the imprint of the log-layer on the near-wall region at high Reynolds number. Inspired by the analysis of Hutchins and Marusic (2007b), we also show correlations computed from spatially high-pass filtered and spatially low-pass filtered instantaneous data at $y^+ \approx 15$ to highlight the separate contribution of small scales and large scales to the total correlation, see Fig. 9(*b*). Filtering is performed in spanwise direction with a finite impulse response (FIR) filter and cutoff wavelengths $\lambda_z^+ = 300$ for the high-pass and $\lambda_z/\delta_0 = 0.2$ for the low-pass filtering operation. The correlation obtained from the spatially low-pass filtered flowfield (dash-dotted line) closely follows the correlation calculated at $y/\delta_0 \approx 0.1$ for large spacing, which shows that the large-scale contribution at $y^+ \approx 15$ can be associated with the imprint of log-layer structures. The correlation computed from the spatially high-pass filtered flow field, on the other hand, recovers the negative peak near the axis (see the dotted line) thus regaining qualitative agreement with low-Reynolds TBL data in absence of scale separation.

Besides the alternating streaks of high- and low-speed fluid, the near-wall region is also populated with vortical structures (Pirozzoli et al., 2008). Together, these two types of coherent motions are responsible for the near-wall turbulence regeneration cycle (Adrian, 2007; Lagha et al., 2011a). The presence of such vortices, mostly oriented in the streamwise direction, explains the observed near-wall distribution of the wall-normal velocity correlation functions in Fig. 8. The global minimum, located at $\Delta z^+ \approx 35$, provides an indication of the average vortex spacing in spanwise direction. In agreement with previous works (Pirozzoli et al., 2008; Lagha et al., 2011b), profiles of streamwise vorticity fluctuations in the wall-normal direction (not shown here) have a local maximum at $y^+ \approx 15$ and a local minimum at $y^+ \approx 5$ in all cases. These heights provide additional insights into the average vortex core location and radial extent (Lagha et al., 2011b,a) and appear insensitive to the Reynolds number in the present simulations.

The spanwise spectra associated with the spanwise velocity correlation functions in Fig. 8 is included in Fig. 10. At $y^+ \approx 15$, see Fig. 10(*a*), the inner-scaled spectra excellently collapse at low wavelengths up to the local peak at $\lambda_z^+ \approx 100$, which is a global peak for case $\mathcal{T}_1$. This confirms the characteristic spanwise spacing of the near-wall streaks inferred from the spatial correlations, which is in good agreement with previous works (Lagha et al., 2011b; Pirozzoli and Bernardini, 2013). The location of the spectral peak for the higher-Reynolds cases, however, is found at much higher wavelengths than $\lambda_z^+ \approx 100$, and is associated with increasing energy levels. This trend is attributed to the imprint of the emergent outer-layer motions, which appear spaced much further apart in spanwise direction (Pirozzoli and Bernardini, 2011). Their approximate spacing is deduced from the spectra at $y/\delta_0 \approx 0.1$, which is shown in Fig. 10(*b*) in outer scaling. As observed, all spectra exhibit a peak at $\lambda_z \approx 0.7\delta_0$ that reveals the average spacing of outer-layer structures. While the peak energy is higher for case $\mathcal{T}_3$, the fact that the corresponding wavelength remains unaffected by Reynolds number indicates its negligible impact on the width of turbulent structures away from the wall. This observation is in agreement with the experimental results of Hutchins and Marusic (2007a) and Bross et al. (2021). Fig. 10(*b*) also highlights the collapse of the spectral distributions for cases $\mathcal{T}_2$ and $\mathcal{T}_3$ along the inertial subrange, which extends for over a decade with close $\kappa_z^{-5/3} = (2\pi/\lambda_z)^{-5/3}$ scaling characteristic of local isotropy (indicated with a dotted line).

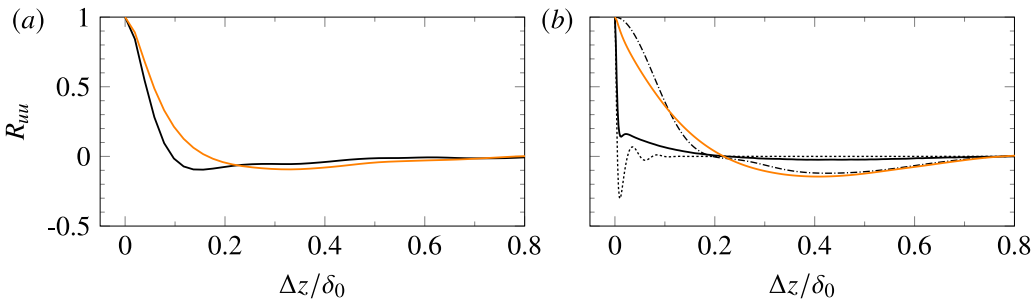

Fig. 9. Spanwise autocorrelation functions of streamwise velocity fluctuations for (*a*) the low-Reynolds case $\mathcal{T}_1$, and (*b*) the high-Reynolds case $\mathcal{T}_3$ at $y^+ \approx 15$ (black solid line) and $y/\delta_0 \approx 0.1$ (orange line). Panel (*b*) additionally includes the correlation computed from the spatially high-pass filtered flowfield (dotted line) and the spatially low-pass filtered flowfield (dash-dotted line) at $y^+ \approx 15$. (For interpretation of the references to color in this figure legend, the reader is referred to the web version of this article.)

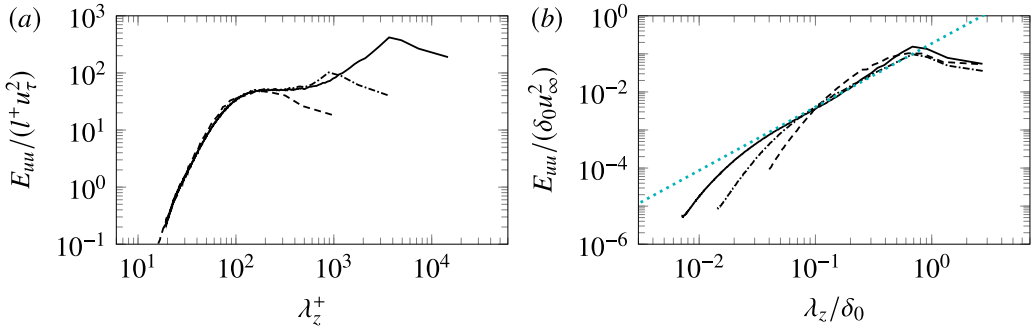

Fig. 10. Spanwise spectra of streamwise velocity fluctuations at (*a*) $y^+ \approx 15$ in inner scaling, and (*b*) $y/\delta_0 \approx 0.1$ in outer scaling. The blue dotted line in (*b*) indicates $\kappa_z^{-5/3} = (2\pi/\lambda_z)^{-5/3}$ scaling.

The characteristic size of turbulent structures is further established by means of the corresponding streamwise and spanwise integral length scales, which are reported in Fig. 11 for all cases. Length scales are here defined as the area between the corresponding correlation function and the isoline $R_{\alpha\alpha} = 0.05$ (Pirozzoli and Bernardini, 2011). The largest streamwise length scales, as shown in Fig. 11(*a*) to (*c*), are clearly associated with the streamwise velocity component (indicated with upward pointing triangles). For the low-Reynolds case $\mathcal{T}_1$, the maximum value of the corresponding scale distribution for this variable is found at $y^+ \approx 15$ and is related to the near-wall streaks. For the other cases, however, there is a scale increase from the wall towards the quasi-log layer, where the peak value is found at $y/\delta_0 \approx 0.1$–0.2. This scale increase is related to the emergent coherent structures in this region, whose mean streamwise elongation is also Reynolds number dependent. As observed, the largest length-scales are found for the high-Reynolds case $\mathcal{T}_3$ which evidences the enlargement of the outer-layer motions with increasing Reynolds number. The corresponding values, which exceed $1.3\delta_0$ at $y/\delta_0 \approx 0.1$, are slightly lower than those experimentally measured by Ganapathisubramani (2007) on a Mach 2.0 TBL at $Re_\tau = 5800$, where the peak value was attained at $y/\delta_0 \approx 0.4$. This could be attributed to the lower Reynolds number of case $\mathcal{T}_3$ compared to the experiments. In Fig. 11(*c*), an emerging local peak is visible at approximately half the boundary layer thickness, and this peak could eventually become global at higher Reynolds numbers. Regarding the streamwise scales associated with the temperature field, indicated with circles in Fig. 11(*a*) to (*c*), they follow the same trend as those for the streamwise velocity, albeit with approximately half the magnitude. This is in very good agreement with the observations of Pirozzoli and Bernardini (2011). The cross-stream velocity components, in turn, exhibit much smaller streamwise length scales, with comparable values ranging from $0.1\delta_0$ to $0.3\delta_0$. In addition, they appear weakly dependent on the Reynolds number, with slightly lower values measured for the high-Reynolds case $\mathcal{T}_3$.

Spanwise length scales for the considered variables are included in Fig. 11(*d*) to (*f*). In all cases, the streamwise velocity, spanwise velocity and temperature scale distributions exhibit a steep rise near the wall, and they progressively relax towards values between $0.2\delta_0$ to $0.3\delta_0$ within half the boundary layer thickness. Interestingly, the aforementioned scale distributions appear to overlap at high Reynolds number, see Fig. 11(*f*) for case $\mathcal{T}_3$. At low Reynolds number, where energetic outer-layer structures are absent, the reported scale distributions are visibly different, see Fig. 11(*d*) for case $\mathcal{T}_1$, and the largest scales are associated with the spanwise velocity. In terms of the wall-normal velocity, its corresponding scales present a different behavior than the rest. As observed, they first exhibit a moderate increase near the wall in all cases, which becomes steeper in the outer part of the boundary layer where the scales become the largest.

Another aspect connected to the turbulence structure in TBL flows involves the presence of confined zones with relatively uniform streamwise momentum, the so-called uniform momentum regions (UMZs). Adrian et al. (2000) attributed UMZs to coherent hairpin vortices in the flow, which tend to align in streamwise direction and form packets with similar convection speeds. Within this paradigm, thin regions of high $\partial u/\partial y$ appear due to the continuous passage of hairpin heads, which translates into wall-normal step-like jumps in the instantaneous streamwise momentum rather than a smooth variation (de Silva et al., 2016). More recently, the experimental work of Laskari et al. (2018) linked the existence of UMZs to different large-scale events in the quasi-logarithmic layer, which meander in spanwise direction and generate instantaneous low- and high-momentum regions across the measurement plane.

The presence of UMZs and their dependence on the Reynolds number is well documented for incompressible TBLs (Adrian et al., 2000; de Silva et al., 2016; Laskari et al., 2018) but very few studies are available for compressible TBLs. The experimental works of Williams et al. (2018) and Bross et al. (2021) are among the few studies that provide evidence for the presence of UMZs in high-speed TBLs, which appear to be similar to their incompressible counterparts. More recently, Cogo et al. (2022) also observed a zonal distribution for the static temperature in their DNS data of high-speed TBLs with heat transfer. The

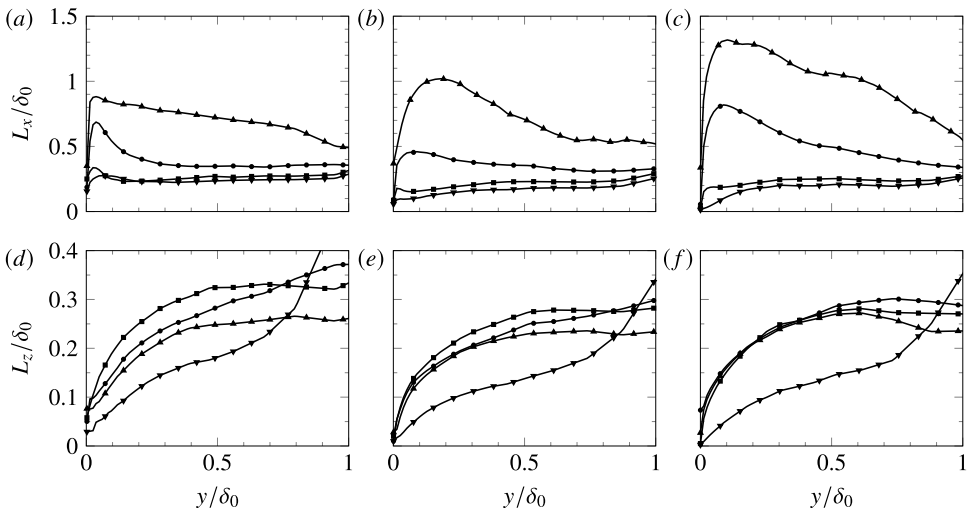

Fig. 11. Integral length scale distributions measured in the streamwise direction (L_x, top panels) and spanwise direction (L_z, bottom panels) for: (*a*), (*d*) case $\mathcal{T}_1$; (*b*), (*e*) case $\mathcal{T}_2$; (*c*), (*f*) case $\mathcal{T}_3$. Marker legend: (▲) streamwise velocity, (▼) wall-normal velocity, (■) spanwise velocity, (●) temperature.

present LES database offers a unique opportunity to further support these claims as well as effectively quantify Reynolds number effects on the resulting number of UMZs, which has not been yet documented for compressible TBLs.

The streamwise velocity u/u_∞ as well as the static temperature T/T_∞ are therefore considered for the detection of uniform zones (UZs), which proceeds as follows. First, the quantity of interest is sampled within a streamwise–wall-normal slice to generate its corresponding (instantaneous) probability density function (PDF). The required bins for the construction of the PDF are defined in steps of $0.5u_\tau$ for $u/u_\infty \in [0, 1.05]$. The associated bin size for $T/T_\infty \in [0.95, T_w/T_\infty]$, in turn, is selected so as to match the number of bins employed for u/u_∞. Once the target PDFs are assembled, a peak detection algorithm identifies the location of the various peaks within each PDF as well as the least probable value between peaks. The resulting number of peaks thus corresponds to the number of UZs for the quantity of interest in the considered slice, while the least probable values between the detected peaks define the boundaries of the UZs. The parameter set for the peak detection algorithm is adopted from Laskari et al. (2018) and corresponds to a minimum peak height of 0.3, a minimum prominence (i.e., distance from neighboring values) of 0.05, and at least two bins between adjacent peaks.

For an optimum evaluation of UZs, the flow above the turbulent/non-turbulent interface (TNTI) is excluded from the analysis. This is required to prevent the free-stream velocity from creating a dominant peak in the corresponding PDF that would inhibit the detection of other peaks in its vicinity (de Silva et al., 2016). The employed definition for the TNTI is adopted from Cogo et al. (2022) and is based on the square of the momentum defect Δp induced by the TBL, i.e,

$$\Delta \mathrm{p} = \frac{(\rho u - \rho_\infty u_\infty)^2 + (\rho v - \rho_\infty v_\infty)^2}{(\rho_\infty u_\infty)^2 + (\rho_\infty v_\infty)^2} = 0.001. \tag{8}$$

In addition, the region below $y^+ = 100$ is also excluded for consistency with experimental datasets, since this region is often unavailable in experiments (de Silva et al., 2016). In streamwise direction, the considered domain is also finite to prevent the resulting PDF from being smoothed out (de Silva et al., 2016). Following Laskari et al. (2018), we consider a length of approximately $2600l^+$ in streamwise direction and centered around $x/\delta_{0,in} = 40$.

Fig. 12(*a*) includes an example of an instantaneous streamwise velocity field for case $\mathcal{T}_3$ where the region considered for the detection of UZs is outlined in blue. The boundaries of the detected UZs are indicated in gray, and the TNTI is shown in black. As observed, the identified boundaries of the UZs are in very good qualitative agreement with the instantaneous flow organization, which conforms to a zonal structure. The corresponding instantaneous PDF of the sampling region of Fig. 12(*a*) is included in Fig. 12(*b*) and shows the three distinct peaks that correspond to the modal velocities of the identified UZs (Adrian et al., 2000).

To accurately assess Reynolds number effects on the number of UZs, we consider two slices per instantaneous snapshot, which leads to an ensemble of ∼500 slices per case. The extracted slices within one snapshot are separated over a distance $1.3\delta_0$ in spanwise direction to ensure proper data decorrelation. The corresponding number of UZs is then identified for each slice, and the PDF of the number of UZs is assembled per variable and for each of the investigated TBLs. The resulting PDFs are shown in Fig. 13(*a*) and confirm the observation of de Silva et al. (2016) for incompressible wall-bounded flows that the corresponding number of UZs increases with the Reynolds number. This is not only valid for the streamwise velocity (shown in black) but also for the temperature field (shown in red), which exhibits an average factor of 1.4 more zones than the streamwise velocity. This value is close to the ∼1.6 factor reported by Cogo et al. (2022). We also note that the PDF for the streamwise velocity field of $\mathcal{T}_2$ is in very good agreement with the corresponding PDF for the lowest Reynolds case of de Silva et al. (2016) ($Re_\tau \approx 1200$) which suggests that the UZs are not strongly affected by compressibility.

Fig. 13(*b*) shows the variation of the average number of UZs ($\overline{N}_{UZ}$) with Re_τ for the cases considered, with black and red markers distinguishing between streamwise velocity and temperature data. As observed, both distributions exhibit an increase with Reynolds number that conforms with the logarithmic trend derived by de Silva et al. (2016) from incompressible streamwise velocity data, which is indicated with a dashed line. This further supports the intrinsic relation between UZs and outer-layer motions, and confirms the negligible influence of compressibility effects on the UZ characteristics. Note that the actual value of $\overline{N}_{UZ}$ for the streamwise velocity appears slightly underpredicted compared to the incompressible data; however, the analysis should only concern trends rather than absolute values, and these appear insensitive to the employed parameter set in the peak search algorithm (confirmed with a separate parametric study). As previously stated, the employed parameters were adopted from previous works and modifications to deliberately match $\overline{N}_{UZ}$ with reported values in literature were not attempted.

Before concluding this section, we consider the instantaneous flow organization to provide a visual impression of the above-described turbulent structures. Streamwise velocity fluctuations are shown in Fig. 14 at two wall-parallel planes, $y^+ \approx 15$ and $y/\delta_0 \approx 0.1$, to illustrate

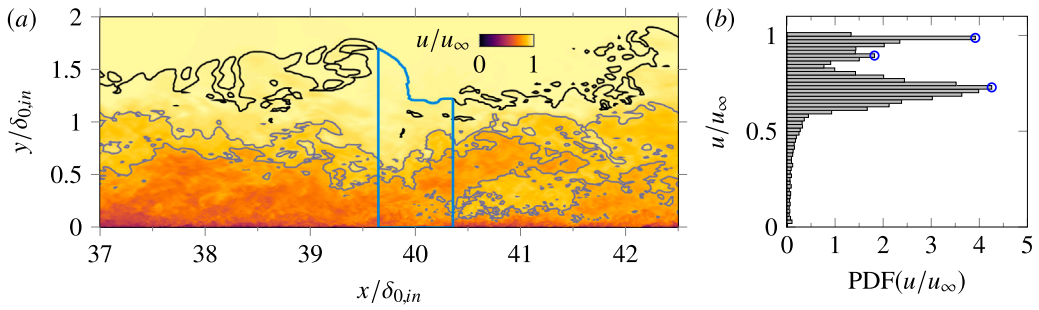

Fig. 12. (*a*) Instantaneous impression of the streamwise velocity field for case $\mathcal{T}_3$, and (*b*) corresponding PDF of the streamwise velocity magnitude. In (*a*), the TNTI and the edge of the identified UZs are respectively indicated with black and gray lines, while the region considered for the analysis of UZs is outlined in blue. In (*b*), peak values identified with the peak search algorithm are indicated with blue circles. (For interpretation of the references to color in this figure legend, the reader is referred to the web version of this article.)

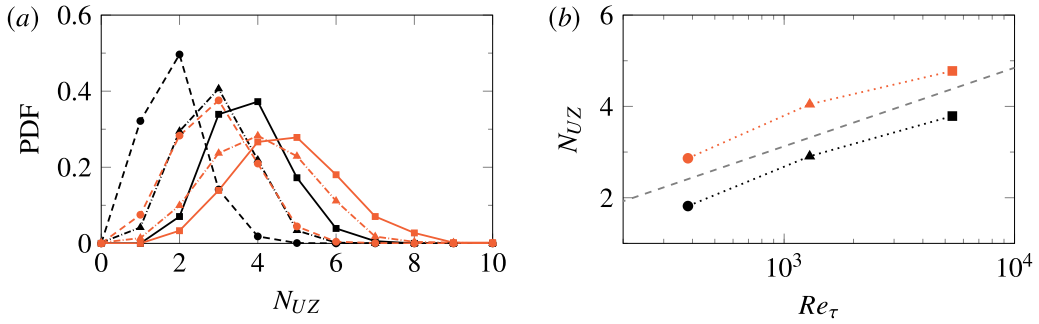

Fig. 13. (*a*) PDF of UZs for the investigated TBLs, and (*b*) evolution of the average number of UZs with Re_τ. Color legend: (black) streamwise velocity, (red) static temperature. (For interpretation of the references to color in this figure legend, the reader is referred to the web version of this article.)

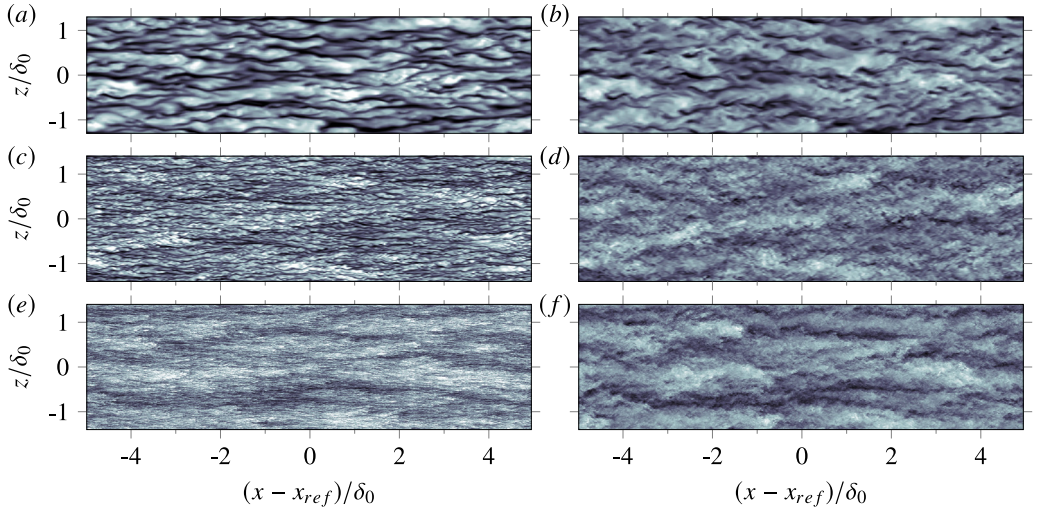

Fig. 14. Instantaneous streamwise velocity field at $y^+ \approx 15$ (left panels) and $y/\delta_0 \approx 0.1$ (right panels): (*a*) – (*b*) case $\mathcal{T}_1$; (*c*) – (*d*) case $\mathcal{T}_2$; (*e*) – (*f*) case $\mathcal{T}_3$. Contour levels from $u'/u_\infty = -0.25$ (dark shade) to $u'/u_\infty = 0.25$ (light shade).

the emerging scale separation and associated scale interaction with increasing Reynolds number. At $y^+ \approx 15$, see the left panels of Fig. 14, the characteristic streaky pattern of low- and high-momentum flow is present in all cases. However, since these structures become progressively finer with Reynolds number, they are hardly visible in Fig. 14(*e*) for case $\mathcal{T}_3$. At $y/\delta_0 \approx 0.1$, in contrast, the corresponding velocity structures for this case are much larger and recognizable, see Fig. 14(*f*). In addition, they leave a very distinct signature near the wall, since the large-scale fluctuations in Fig. 14(*e*) conform closely to the large-scale structures in Fig. 14(*f*). This illustrates the correspondence between the log-layer and the near-wall region, which is not so apparent for the moderate Reynolds case $\mathcal{T}_2$ when comparing Fig. 14(*c*) and (*d*). For the low-Reynolds case $\mathcal{T}_1$, the observed structures at $y/\delta_0 \approx 0.1$ exhibit similar sizes to those in the viscous sub-layer, see Fig. 14(*a*) and (*b*), which is expected in the absence of scale separation.

A three-dimensional view of velocity structures is included in Fig. 15 for each case, the Reynolds number increasing from top to bottom. In addition, the swirling strength criterion λ_{ci} is employed to reveal the corresponding vortical structures (Zhou et al., 1999). As observed, velocity streaks with similar spanwise spacing are present in all cases. For the low-Reynolds case $\mathcal{T}_1$, see Fig. 15(*a*), the corresponding vortical structures are of considerable size and resemble hairpin vortices. The higher Reynolds cases $\mathcal{T}_2$ and $\mathcal{T}_3$, in contrast, exhibit vortical structures of much smaller size, see Fig. 15(*b*) and (*c*), which have not been

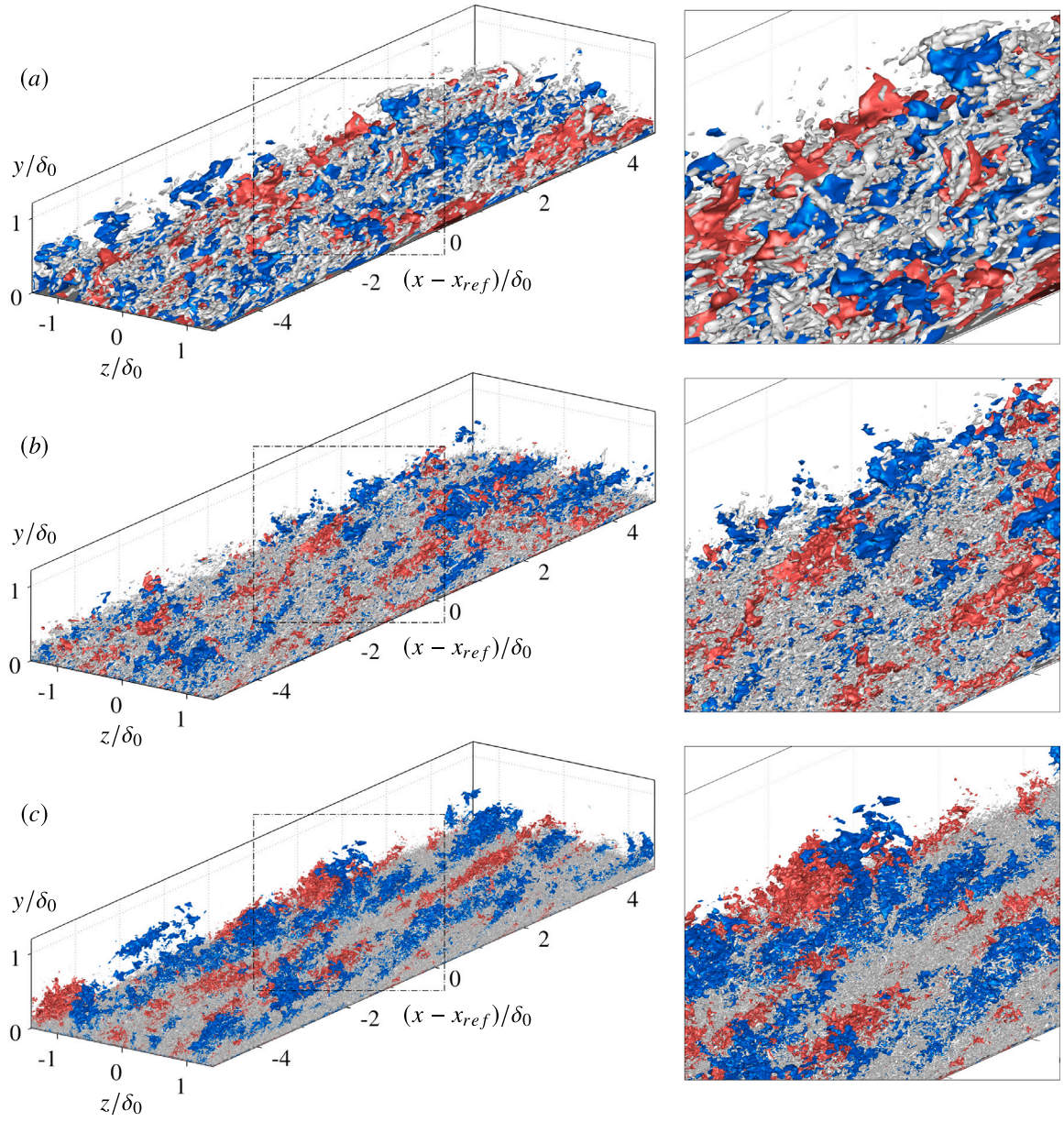

Fig. 15. Instantaneous three-dimensional flow organization for (*a*) case $\mathcal{T}_1$, (*b*) case $\mathcal{T}_2$, and (*c*) case $\mathcal{T}_3$. Iso-surfaces correspond to $u'/u_\infty = -0.12$ (blue), $u'/u_\infty = 0.12$ (red) and $\lambda_{ci} = 2\overline{\lambda}_{ci}$ (gray), where $\overline{\lambda}_{ci}$ is the average value of the swirling strength at $y/\delta_0 = 0.1$. Dash-dotted lines indicate the location of the close-up view provided on the right panels. (For interpretation of the references to color in this figure legend, the reader is referred to the web version of this article.)

filtered out by the employed computational grid. In agreement with the observations of Pirozzoli and Bernardini (2011), these small-scale structures exhibit a tubular shape that does not conform to the classical hairpin eddy (see the close-up view on the right panels).

3.4. Thermodynamic statistics

The transport of internal energy, the transfer between kinetic and internal energy, and the corresponding fluctuations of the thermodynamic state properties play important roles in compressible turbulence. As a consequence, an accurate characterization of thermodynamic fluctuations and their mutual interaction with the velocity field is necessary for model development.

Fig. 16 reports fluctuation profiles of thermodynamic variables in both inner scaling (left panels) and semi-local scaling (right panels). As observed, the isothermal boundary condition inhibits temperature fluctuations at the wall, which leads to density and pressure fluctuations of similar normalized magnitudes in the linear sub-layer. Additionally, their fluctuation intensity at the wall is observed to progressively increase with Reynolds number, see Fig. 16(*a*) and (*c*). This is a consequence of the modulating influence of the outer layer motions (Pirozzoli and Bernardini, 2011). Experimental evidence suggest a logarithmic increase of the inner-scaled wall-pressure fluctuations with Re_τ. While the corresponding values for cases $\mathcal{T}_1$ and $\mathcal{T}_2$ conform well with the empirical correlation of Farabee and Casarella (1991), within 2% and 7% error from the respective predicted values, inner-scaled wall-pressure fluctuations for $\mathcal{T}_3$ exceed the predicted values by a slightly larger margin. This is attributed to the spurious noise generated by the digital filter, which increases in magnitude with the inflow Reynolds number and requires long distances to relax (Ceci et al., 2022).

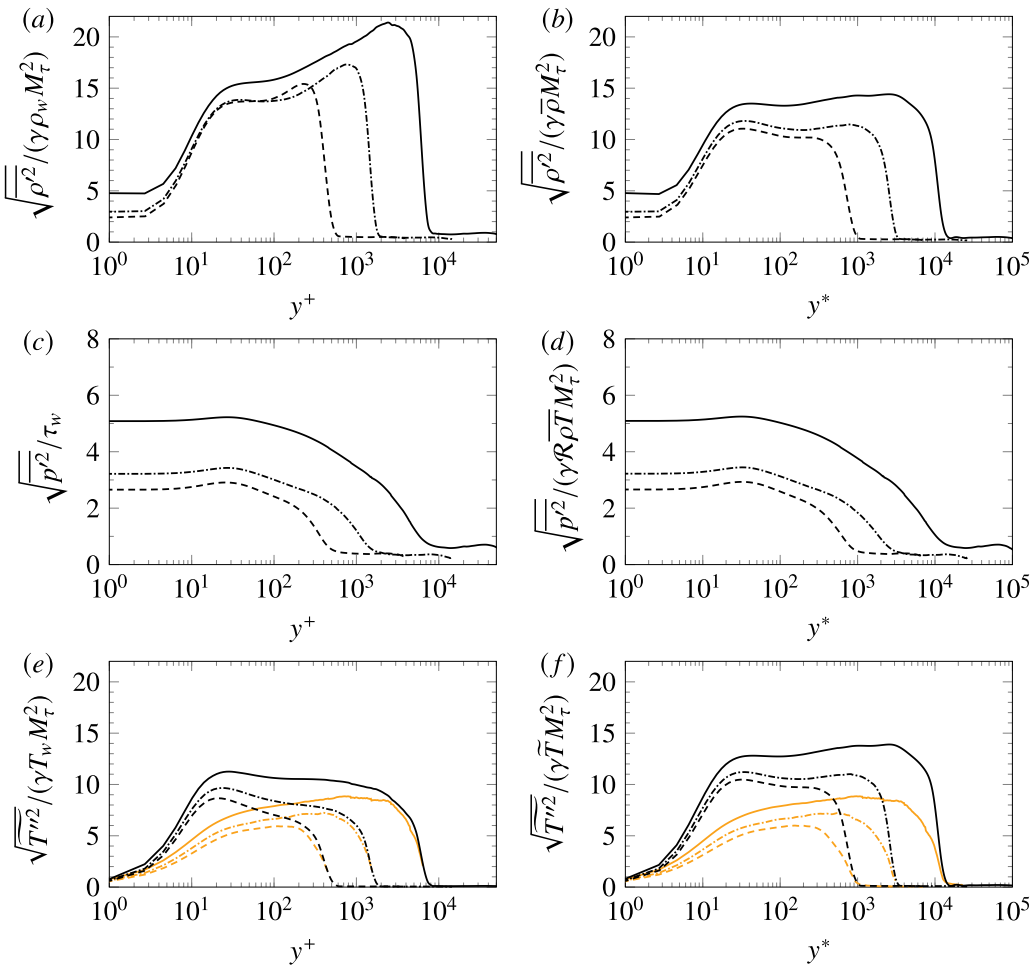

Fig. 16. Wall-normal distribution of the inner-scaled (left panels) and semi-locally scaled (right panels) thermodynamic fluctuations: $(a)-(b)$ density; $(c)-(d)$ temperature; $(e)-(f)$ pressure. The distribution of total temperature fluctuations is additionally included in panels (e) and (f) (orange lines), and $M_\tau = u_\tau(\gamma R T_w)^{-1/2}$. (For interpretation of the references to color in this figure legend, the reader is referred to the web version of this article.)

Away from the wall, inner-scaled temperature fluctuations attain their peak value in the buffer layer, see Fig. 16(e), while the inner-scaled density fluctuations in Fig. 16(a) clearly peak at the boundary layer edge. This is a consequence of the mean temperature and density distributions in wall-normal direction, which stimulate their corresponding fluctuations in opposite ways (Cogo et al., 2022). If mean-property variation effects are taken into account, for instance, by considering the semi-local scaling shown in Fig. 16(b) and (f), temperature and density fluctuations exhibit very similar behavior across the boundary layer (except for the near-wall region). This highlights the close relation between these two variables in compressible TBLs. The resulting fluctuation profiles are almost flat from the upper end of the buffer layer until the boundary layer edge, where a peak seems to emerge at high Reynolds number. In addition, the intensity of the fluctuations across the boundary layer is also dependent on the Reynolds number.

The fluctuating pressure, on the other hand, is not modulated by mean-property variation effects because the mean-pressure is approximately constant. At the same time, the corresponding fluctuations across the layer do not resemble those associated with the temperature and density in any of the considered scalings, which indicates a lower degree of correlation, i.e., higher decoupling, between them (see next paragraph). As observed in Fig. 16(c) and (d), pressure fluctuations are largest in the near-wall region, where the strongest vorticity fluctuations are found, and progressively decrease along the quasi-logarithmic region and towards the free-stream flow. While their behavior is qualitatively similar for the different TBLs considered, the intensity of the pressure fluctuations is clearly sensitive to the Reynolds number across the whole layer, being highest for case $\mathcal{T}_3$.

The correlation coefficients between thermodynamic variables are shown in Fig. 17, where no systematic Reynolds number effects are observed. The density–temperature correlation of Fig. 17(a) confirms the close relation between these two variables, with $R_{\rho T}$ being approximately -0.9 in the buffer layer and continuing to approach -1 with increasing wall-distance. The fact that they are anti-correlated clearly depicts the non-isentropic behavior of the thermodynamic fluctuations inside the boundary layer. Beyond the boundary layer edge, in turn, the correlation changes drastically and approaches unity within half a boundary layer thickness. This is a consequence of the acoustic disturbances dominating the free-stream flow, which are of isentropic nature. The density–pressure correlation, see Fig. 17(b), is unity at the wall due to the isothermal boundary condition, which inhibits temperature fluctuations. The correlation then drops to a value of about 0.2 within the buffer layer and increases slightly towards the intermittent boundary layer edge, where it levels off and starts to decrease again. Similar as for the density–temperature correlation, the density–pressure correlation changes trend outside the TBL and reaches unity within $1.5\delta_0$ from the wall. This is also the case for the pressure–temperature correlation in Fig. 17(c). Interestingly, this correlation is positive near the wall but changes sign inside the boundary layer. As observed, a local maximum of approximately 0.4 is first attained in the viscous sub-layer and is followed by a progressive decrease that crosses $R_{pT} = 0$ at $y/\delta_0 \approx 0.3$. The correlation then levels off to a value of about -0.3 to -0.4 near the edge of the boundary layer.

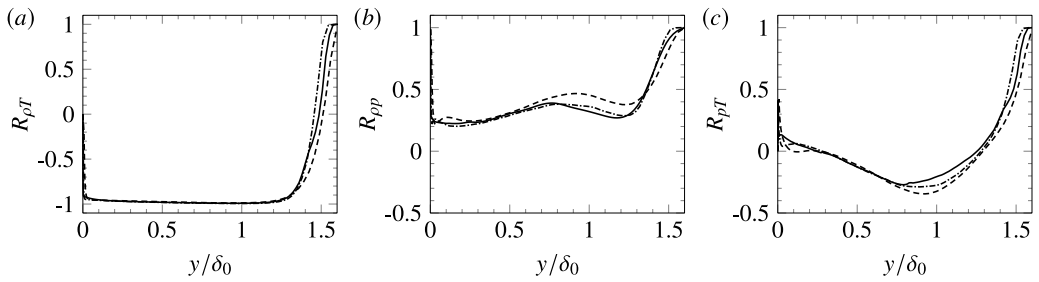

Fig. 17. Wall-normal distribution of the correlation coefficients between (*a*) density and temperature, (*b*) density and pressure, and (*c*) pressure and temperature.

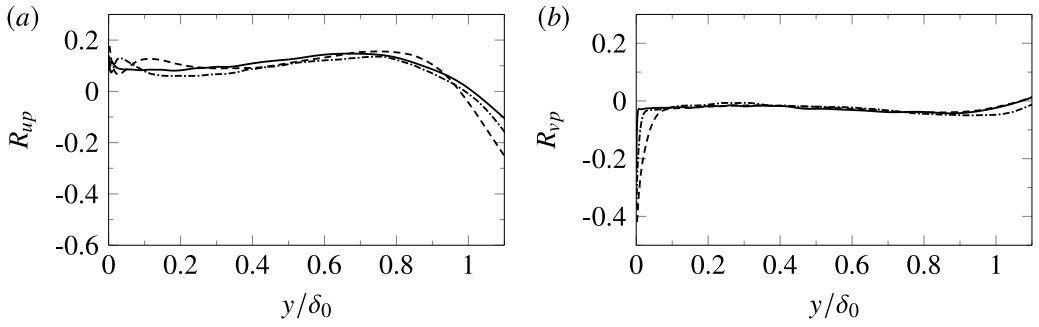

Fig. 18. Wall-normal distribution of the correlation coefficients between (*a*) pressure and streamwise velocity, and (*b*) pressure and wall-normal velocity.

The turbulent pressure diffusion is analyzed in Fig. 18(*a*) and (*b*), where the coefficients for the pressure–streamwise velocity and pressure–wall-normal velocity correlations are respectively shown. In agreement with the DNS data of Gerolymos and Vallet (2014) for compressible channel flows, both correlations are very weak within the boundary layer except for R_{vp} in the near-wall region $y^+ \lesssim 10$. This local increase is associated with considerable transport of turbulence kinetic energy (TKE) away from the wall, since the corresponding pressure-diffusion term in the TKE transport equation is $-\partial_y[\overline{p'v''}]$ (Guarini et al., 2000). Furthermore, R_{up} also becomes increasingly negative at the boundary layer edge, see Fig. 18(*a*), which is attributed to outward excursions of low-speed rotational fluid towards the free-stream. The pressure–velocity correlations do not exhibit any strong or consistent Reynolds number dependence.

The relationship between the streamwise velocity and the temperature fields is considered next. Under the assumption of constant mean total temperature and negligible total temperature fluctuations, Morkovin (1962) proposed a series of relations for an equilibrium zero-pressure-gradient TBL over an adiabatic wall, known collectively as the strong Reynolds analogy (SRA). Three of these relations are

$$\frac{\sqrt{\widetilde{T''^2}}/\widetilde{T}}{(\gamma-1)M^2\sqrt{\widetilde{u''^2}}/\widetilde{u}} \approx 1, \tag{9}$$

$$R_{uT} = \frac{\widetilde{u''T''}}{\sqrt{\widetilde{u''^2}}\sqrt{\widetilde{T''^2}}} \approx -1, \tag{10}$$

$$Pr_t = \frac{[-\overline{\rho u''v''}](\partial\widetilde{T}/\partial y)}{[-\overline{\rho v''T''}](\partial\widetilde{u}/\partial y)} \approx 1, \tag{11}$$

with $M^2 = \widetilde{u}^2/\gamma\mathcal{R}\widetilde{T}$.

These relations have been extensively employed for modeling purposes despite their rather questionable agreement with experimental or numerical data (Guarini et al., 2000; Pirozzoli and Bernardini, 2011; Duan et al., 2011; Huang et al., 2022). For instance, the assumption of constant total temperature is a fair approximation for the present quasi-adiabatic LES data (variations do not exceed 1.5% of $T_{0,\infty} = T_w$), while negligible total temperature fluctuations is not. The distribution of total temperature fluctuations in wall-normal direction is also included in Fig. 16(*e*) and (*f*) for the investigated TBLs, where it is clear that $\widetilde{T_0''^2}$ exhibits comparable magnitudes as $\widetilde{T''^2}$.

Evaluation of Eqs. (9)–(11) reflects the aforementioned deviation from the SRA assumptions. For instance, the streamwise velocity–temperature correlations and the turbulent Prandtl number shown in Fig. 19(*a*) and (*b*) are clearly not unity throughout the boundary layer. The distribution for $-R_{uT}$ exhibits a peak value of approximately 0.9 in the buffer layer. In agreement with the DNS data of Pirozzoli and Bernardini (2011), the correlation appears weakly dependent on the Reynolds number near the wall. However, no apparent Reynolds number dependence can be identified above $y/\delta_0 \approx 0.3$, where all correlations exhibit a value between 0.5 and 0.6 before dropping again at the boundary layer edge. The turbulent Prandtl number in Fig. 19(*b*) exhibits a somewhat similar trend as $-R_{uT}$ throughout most of the boundary layer, with values slightly closer to unity (between 0.6 and 0.8). At the edge of the boundary layer, however, its magnitude starts to increase rather than decrease.

The SRA relation (9) is evaluated in Fig. 20(*a*). Interestingly, all cases exhibit a nearly-constant value close to unity within the first half of the boundary layer. However, this is no longer true in the outer region, where all distributions largely overshoot the expected unity value of the SRA paradigm. In view of these deviations, Huang et al. (1995) proposed a so-called modified SRA, in an attempt to improve the agreement with non-adiabatic TBL data. The resulting expression, which takes into account heat fluxes at the wall, is

$$\frac{\sqrt{\widetilde{T''^2}}/\widetilde{T}}{(\gamma-1)M^2\sqrt{\widetilde{u''^2}}/\widetilde{u}} \approx \frac{1}{Pr_t[1-(\partial\widetilde{T_0}/\partial\widetilde{T})]}. \tag{12}$$

We multiply the left-hand side by the denominator on the right-hand side, which leads to a modified-SRA indicator that also predicts unity. This indicator is evaluated in Fig. 20(*b*) and shows clear improvements in the outer layer with respect to the SRA, in very good agreement with previous findings (Guarini et al., 2000; Pirozzoli and Bernardini, 2011; Duan et al., 2011; Huang et al., 2022). Interestingly, the modified-SRA also reveals a weak Reynolds number dependence that is consistent throughout the boundary layer.

As shown by Guarini et al. (2000), an improved expression for the streamwise velocity–temperature correlation can be derived by

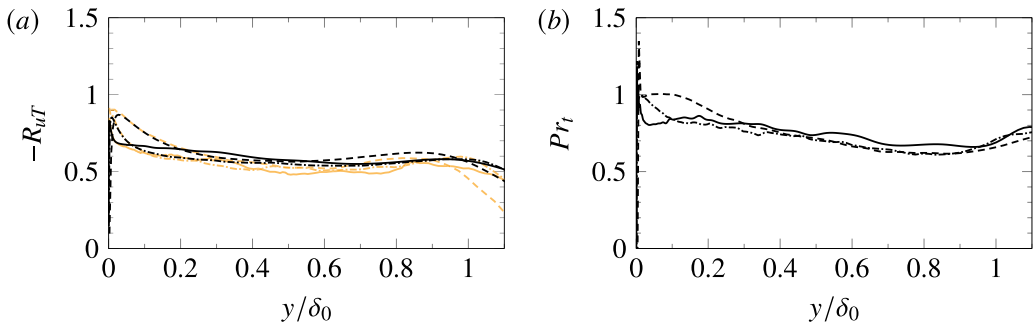

Fig. 19. Wall-normal distribution of (*a*) the correlation coefficient between streamwise velocity and temperature, and (*b*) the turbulent Prandtl number. Orange lines in (*a*) indicate the corresponding distributions obtained with Eq. (14). (For interpretation of the references to color in this figure legend, the reader is referred to the web version of this article.)

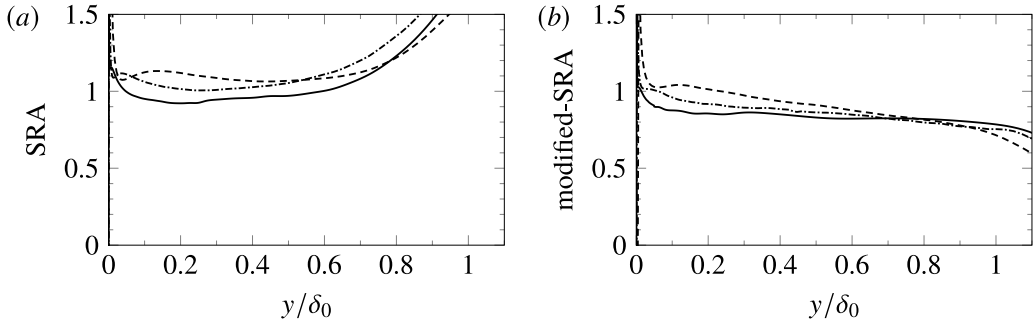

Fig. 20. Evaluation of (*a*) the SRA relation (Eq. (9)), and (*b*) the modified version by Huang et al. (1995) (Eq. (12)).

considering the modified-SRA version of Huang et al. (1995) in the presence of non-negligible total temperature fluctuations. By retaining only those terms that are linear in the fluctuations, total temperature fluctuations can be expressed as

$$\overline{T_0''^2} \approx \overline{T''^2} + \frac{\widetilde{u}^2}{c_p^2}\overline{u''^2} + 2\frac{\widetilde{u}}{c_p}\sqrt{\overline{T''^2}}\sqrt{\overline{u''^2}}R_{uT}. \tag{13}$$

Substituting Eq. (12) into Eq. (13) and solving for R_{uT} yields

$$R_{uT} \approx \frac{[\overline{T_0''^2}/\overline{T''^2} - 1]}{[2Pr_t(1 - \partial\widetilde{T_0}/\partial\widetilde{T})]} - \frac{Pr_t}{2}\left(1 - \frac{\partial\widetilde{T_0}}{\partial\widetilde{T}}\right). \tag{14}$$

This expression is evaluated for the considered TBLs, and the corresponding distributions are included in Fig. 19(*a*) for comparison (orange lines). As observed, they are in very good agreement with the present LES data. This further confirms the relevance of total temperature fluctuations in compressible TBLs as well as the enhanced performance of the modified-SRA relation by Huang et al. (1995), even for quasi-adiabatic wall conditions.

4. Conclusions

We have presented and discussed a database of compressible zero-pressure-gradient turbulent boundary layers (TBLs) that covers more than a decade of friction Reynolds number Re_τ, from 242 to 5554. Reynolds number effects have been quantified on a variety of statistics, starting with the mean and fluctuating skin-friction profiles and velocity statistics up to fourth order. The density-scaled Reynolds stresses exemplary illustrate the influence of Reynolds number on the TBL topology, most notably through a distinct increase in fluctuation intensity for the wall-parallel components with Re_τ. This is a direct effect of the emergent large-scale coherent motions in the near-logarithmic region, which for the high-Reynolds case extends for over a decade of y^+. Furthermore, the total-stress-based scaling proposed by Griffin et al. (2021) was found to improve the collapse of the mean velocity profiles in the buffer layer without increasing the data scatter elsewhere. Improved collapse of the wall-parallel Reynolds stresses and a better alignment of the streamwise stress peak was also found by simply employing the semi-local wall-distance y^* (instead of y^+) as suggested by Huang et al. (1995) and Patel et al. (2015). Regarding the higher-order velocity statistics, the most notable Reynolds number trend is found near the wall where both skewness and flatness increase with increasing Reynolds number. This could be attributed to the stronger footprint of the log-layer structures on the near-wall turbulence, which becomes more intermittent. In addition, we observe a breakdown of Morkovin's hypothesis for third-order velocity statistics, which has been previously reported only for variable-property flows at low Mach number (Patel et al., 2015). We thus believe that this breakdown of Markovin's hypothesis is not a genuine compressibility effect.

Particular attention has also been placed on quantifying the size of the turbulent structures populating the TBL, always with an emphasis on the outer-layer motions at high Reynolds number. Separation of the inner and outer scales of the high-Reynolds case is confirmed upon inspection of the pre-multiplied streamwise energy spectra of streamwise velocity fluctuations, which have a bimodal configuration with an inner peak at $y^+ \approx 15$ and $\lambda_x^+ \approx 700$ and an outer peak at $y/\delta_0 \approx 0.1$ and $\lambda_x/\delta_0 \approx 6$. The associated two-point autocorrelation map with the reference location at $y_{ref}/\delta_0 = 0.2$ also evidences the considerable elongation of the emergent outer-layer motions. The interaction between these structures and the near-wall turbulence is also apparent here, since increased correlation magnitudes extend all the way to the wall. The correlation maps also show that this wall-coherence is established at an oblique angle with respect to the free-stream flow, which implies a forward inclination of the outer-layer structures. The correlation maps for the low- and moderate-Reynolds cases conform well with an inclination of 14° in the outer part of the boundary layer, which corresponds to the value reported by Marusic and Heuer (2007) over a wide range of Reynolds numbers. The high-Reynolds case, in turn, exhibits a slightly smaller inclination above the reference height of approximately 10°. We also note that all correlation maps conform to more shallow angles between 8° and 11° near the wall. In view of this, a line fit of the peak points in wall-normal direction is considered to be a poor representation of the inclination of the correlation map,

and would certainly lead to a smaller inclination angle than 14° in all cases.

The average spanwise spacing of the dominant turbulent structures has been assessed from spanwise autocorrelation functions and related spectra. In all cases, the streamwise velocity correlation calculated at $y^+ \approx 15$ reveals a local minimum at $\Delta z^+ \approx 50$, which provides an indication of the spanwise spacing between adjacent near-wall streaks. However, this minimum is found at a positive correlation value for the high-Reynolds case, which highlights the organizing effect of the log-layer on the near-wall region. The global correlation minimum at $\Delta z^+ \approx 50$ can be recovered by removing the large-scale imprint with a high-pass filter, whereas correlations computed from low-pass filtered data at $y^+ \approx 15$ resemble the typical correlation function of the log-layer structures. In particular the latter has very promising implications for flow control applications as well as for wall modeling in LES.

The spanwise spectra of the unfiltered data at $y^+ \approx 15$ also show the imprint of log-layer structures for the higher-Reynolds case, for which the location of the spectral peak is found at a much higher wavelengths than $\lambda_z^+ \approx 100$. The approximate spacing of the outer-layer motions is deduced from the spectra at $y/\delta_0 \approx 0.1$ where a peak is found at $\lambda_z \approx 0.7\delta_0$ in all cases. While the peak kinetic energy increases at higher Reynolds number, the fact that the corresponding wavelength remains unaltered indicates that the width of turbulent structures away from the wall is essentially independent of Reynolds number. This observation is in very good agreement with the experimental results of Hutchins and Marusic (2007a) and Bross et al. (2021).

The characteristic size of turbulent structures has been further established via the corresponding streamwise and spanwise integral length scales. The largest streamwise length scales are clearly observed for the streamwise velocity of the high-Reynolds case, which exceed a value of $1.3\delta_0$ at $y/\delta_0 \approx 0.1$. The streamwise scales associated with the temperature field are found to follow the same trend as those for the streamwise velocity, albeit with approximately half the magnitude. This is in very good agreement with the observations of Pirozzoli and Bernardini (2011). Regarding the spanwise direction, it is found that the scales for the temperature, streamwise and spanwise velocity fields appear to progressively collapse with increasing Reynolds number throughout the first half of the TBL.

We have also analyzed the Re_τ-sensitivity of uniform momentum regions in the flow (Adrian et al., 2000). We found that the resulting probability density function of the number of zones as well as its evolution with Re_τ agrees well with incompressible data (de Silva et al., 2016). This suggests that uniform momentum zones, which have been associated with outer-layer dynamics (Laskari et al., 2018), are not strongly influenced by compressibility at the considered Mach number.

The last section of the paper has been devoted to the analysis of thermodynamic fluctuations due to their important roles in compressible turbulence. When mean-property variation effects are taken into account, temperature and density fluctuations are found to exhibit very similar behavior across the boundary layer (except for the near-wall region). This highlights the close relation between these two variables in compressible TBLs, which is further confirmed by their correlation coefficient being close to -1 throughout the boundary layer. The fact that they are anti-correlated also reveals the non-isentropic nature of compressible wall-bounded turbulence. The resulting fluctuation profiles for the temperature and density are found to be almost flat from the upper end of the buffer layer until the boundary layer edge, where a peak seems to emerge at high Reynolds number. The fluctuating pressure, on the other hand, is not modulated by mean-property variation effects and the corresponding fluctuations do not resemble those associated with the temperature and density. This indicates a lower degree of correlation, i.e., higher decoupling, between them, which is also confirmed by their corresponding covariances. Pressure fluctuations are largest in the near-wall region, where the strongest vorticity fluctuations are found, and progressively decrease along the quasi-logarithmic region and towards the free-stream flow. While their behavior is qualitatively similar for the different TBLs considered, the intensity of the pressure fluctuations is also clearly sensitive to the Reynolds number across the whole boundary layer.

Finally, the present database demonstrates the deficiencies of the strong Reynolds analogy (SRA), starting with the presence of non-negligible total temperature fluctuations. The modified-SRA relation of Huang et al. (1995), however, shows clear improvements with respect to the SRA. We hope that the data discussed in this paper, which will be made openly accessible, can be employed to develop or to further refine compressible turbulence models as well as turbulence generation methods.

Declaration of competing interest

The authors declare that they have no known competing financial interests or personal relationships that could have appeared to influence the work reported in this paper.

Data availability

The data of the present LES will be made available at https://www.inca-cfd.com.

Acknowledgments

We acknowledge PRACE for awarding us access to HAWK at the High-Performance Computing Center Stuttgart, Germany.

References

Adrian, R.J., 2007. Hairpin vortex organization in wall turbulence. Phys. Fluids 19 (4), 041301.
Adrian, R.J., Meinhart, C.D., Tomkins, C.D., 2000. Vortex organization in the outer region of the turbulent boundary layer. J. Fluid Mech. 422, 1–54.
Bross, M., Scharnowski, S., Kähler, C.J., 2021. Large-scale coherent structures in compressible turbulent boundary layers. J. Fluid Mech. 911.
Ceci, A., Palumbo, A., Larsson, J., Pirozzoli, S., 2022. Numerical tripping of high-speed turbulent boundary layers. Theor. Comput. Fluid Dyn. 36 (6), 865–886.
Choi, H., Moin, P., 2012. Grid-point requirements for large eddy simulation: Chapman's estimates revisited. Phys. Fluids 24 (1), 011702.
Cogo, M., Salvadore, F., Picano, F., Bernardini, M., 2022. Direct numerical simulation of supersonic and hypersonic turbulent boundary layers at moderate-high Reynolds numbers and isothermal wall condition. J. Fluid Mech. 945, A30.
de Silva, C.M., Hutchins, N., Marusic, I., 2016. Uniform momentum zones in turbulent boundary layers. J. Fluid Mech. 786, 309–331.
Duan, L., Beekman, I., Martin, M.P., 2011. Direct numerical simulation of hypersonic turbulent boundary layers. part 3. Effect of Mach number. J. Fluid Mech. 672, 245–267.
Elsinga, G.E., Adrian, R.J., Van Oudheusden, B.W., Scarano, F., 2010. Three-dimensional vortex organization in a high-Reynolds-number supersonic turbulent boundary layer. J. Fluid Mech. 644, 35–60.
Farabee, T.M., Casarella, M.J., 1991. Spectral features of wall pressure fluctuations beneath turbulent boundary layers. Phys. Fluids A 3 (10), 2410–2420.
Ganapathisubramani, B., 2007. Statistical properties of streamwise velocity in a supersonic turbulent boundary layer. Phys. Fluids 19 (9), 098108.
Ganapathisubramani, B., Clemens, N.T., Dolling, D.S., 2006. Large-scale motions in a supersonic turbulent boundary layer. J. Fluid Mech. 556, 271–282.
Gatski, T.B., Bonnet, J.-P., 2013. Compressibility, Turbulence and High Speed Flow. Academic Press.
Gaviglio, J., 1987. Reynolds analogies and experimental study of heat transfer in the supersonic boundary layer. Int. J. Heat Mass Transfer 30 (5), 911–926.
Gerolymos, G.A., Vallet, I., 2014. Pressure, density, temperature and entropy fluctuations in compressible turbulent plane channel flow. J. Fluid Mech. 757, 701–746.
Griffin, K.P., Fu, L., Moin, P., 2021. Velocity transformation for compressible wall-bounded turbulent flows with and without heat transfer. Proc. Natl. Acad. Sci. 118 (34), e2111144118.
Guarini, S.E., Moser, R.D., Shariff, K., Wray, A., 2000. Direct numerical simulation of a supersonic turbulent boundary layer at mach 2.5. J. Fluid Mech. 414, 1–33.
Hadjadj, A., Ben-Nasr, O., Shadloo, M.S., Chaudhuri, A., 2015. Effect of wall temperature in supersonic turbulent boundary layers: A numerical study. Int. J. Heat Mass Transfer 81, 426–438.
Hickel, S., Egerer, C.P., Larsson, J., 2014. Subgrid-scale modeling for implicit large eddy simulation of compressible flows and shock-turbulence interaction. Phys. Fluids 26 (10), 106101.

Hopkins, E.J., Inouye, M., 1971. An evaluation of theories for predicting turbulent skin friction and heat transfer on flat plates at supersonic and hypersonic Mach numbers. AIAA J. 9 (6), 993–1003.
Hoyas, S., Jiménez, J., 2006. Scaling of the velocity fluctuations in turbulent channels up to Re_τ=2003. Phys. Fluids 18 (1), 011702.
Huang, P.G., Coleman, G.N., Bradshaw, P., 1995. Compressible turbulent channel flows: DNS results and modelling. J. Fluid Mech. 305, 185–218.
Huang, J., Duan, L., Choudhari, M.M., 2022. Direct numerical simulation of hypersonic turbulent boundary layers: effect of spatial evolution and Reynolds number. J. Fluid Mech. 937.
Hutchins, N., Marusic, I., 2007a. Evidence of very long meandering features in the logarithmic region of turbulent boundary layers. J. Fluid Mech. 579, 1–28.
Hutchins, N., Marusic, I., 2007b. Large-scale influences in near-wall turbulence. Phil. Trans. R. Soc. A 365 (1852), 647–664.
Jiménez, J., Pinelli, A., 1999. The autonomous cycle of near-wall turbulence. J. Fluid Mech. 389, 335–359.
Lagha, M., Kim, J., Eldredge, J.D., Zhong, X., 2011a. Near-wall dynamics of compressible boundary layers. Phys. Fluids 23 (6), 065109.
Lagha, M., Kim, J., Eldredge, J.D., Zhong, X., 2011b. A numerical study of compressible turbulent boundary layers. Phys. Fluids 23 (1), 015106.
Laguarda, L., Hickel, S., 2023. Analysis of improved digital filter inflow generation methods for compressible turbulent boundary layers. Comput. Fluids (accepted for publication).
Laskari, A., de Kat, R., Hearst, R.J., Ganapathisubramani, B., 2018. Time evolution of uniform momentum zones in a turbulent boundary layer. J. Fluid Mech. 842, 554–590.
Marusic, I., Heuer, W.D.C., 2007. Reynolds number invariance of the structure inclination angle in wall turbulence. Phys. Rev. Lett. 99 (11), 114504.
Morkovin, M.V., 1962. Effects of compressibility on turbulent flows. Méc. Turbul. 367 (380), 26.
Patel, A., Peeters, J.W.R., Boersma, B.J., Pecnik, R., 2015. Semi-local scaling and turbulence modulation in variable property turbulent channel flows. Phys. Fluids 27 (9), 095101.
Pirozzoli, S., Bernardini, M., 2011. Turbulence in supersonic boundary layers at moderate Reynolds number. J. Fluid Mech. 688, 120–168.
Pirozzoli, S., Bernardini, M., 2013. Probing high-Reynolds-number effects in numerical boundary layers. Phys. Fluids 25 (2), 021704.
Pirozzoli, S., Bernardini, M., Grasso, F., 2008. Characterization of coherent vortical structures in a supersonic turbulent boundary layer. J. Fluid Mech. 613, 205–231.
Pirozzoli, S., Grasso, F., Gatski, T.B., 2004. Direct numerical simulation and analysis of a spatially evolving supersonic turbulent boundary layer at M=2.25. Phys. Fluids 16 (3), 530–545.
Poinsot, T.J., Lele, S.K., 1992. Boundary conditions for direct simulations of compressible viscous flows. J. Comput. Phys. 101 (1), 104–129.
Ringuette, M.J., Wu, M., Martin, M.P., 2008. Coherent structures in direct numerical simulation of turbulent boundary layers at Mach 3. J. Fluid Mech. 594, 59–69.
Schlatter, P., Li, Q., Brethouwer, G., Johansson, A.V., Henningson, D.S., 2010. Simulations of spatially evolving turbulent boundary layers up to Re_θ=4300. Int. J. Heat Fluid Flow 31 (3), 251–261.
Schlatter, P., Örlü, R., 2010. Assessment of direct numerical simulation data of turbulent boundary layers. J. Fluid Mech. 659, 116–126.
Schoenherr, K.E., 1932. Resistance of flat surfaces moving through a fluid. Trans. Soc. Nav. Archit. Mar. Eng. 40, 279–313.
Shahab, M.F., Lehnasch, G., Gatski, T.B., Comte, P., 2011. Statistical characteristics of an isothermal, supersonic developing boundary layer flow from DNS data. Flow Turbul. Combust. 86 (3), 369–397.
Smits, A.J., Dussauge, J.-P., 2006. Turbulent Shear Layers in Supersonic Flow. Springer Science & Business Media.
Smits, A.J., Matheson, N., Joubert, P.N., 1983. Low-Reynolds-number turbulent boundary layers in zero and favorable pressure gradients. J. Ship Res. 27 (03), 147–157.
Townsend, A.A., 1961. Equilibrium layers and wall turbulence. J. Fluid Mech. 11 (1), 97–120.
Trettel, A., Larsson, J., 2016. Mean velocity scaling for compressible wall turbulence with heat transfer. Phys. Fluids 28 (2), 026102.
Van Driest, E.R., 1956. The Problem of Aerodynamic Heating. Institute of the Aeronautical Sciences.
Veloudis, I., Yang, Z., McGuirk, J.J., Page, G.J., Spencer, A., 2007. Novel implementation and assessment of a digital filter based approach for the generation of LES inlet conditions. Flow Turbul. Combust. 79 (1), 1–24.
Wenzel, C., Selent, B., Kloker, M., Rist, U., 2018. DNS of compressible turbulent boundary layers and assessment of data/scaling-law quality. J. Fluid Mech. 842, 428–468.
Williams, O.J.H., Sahoo, D., Baumgartner, M.L., Smits, A.J., 2018. Experiments on the structure and scaling of hypersonic turbulent boundary layers. J. Fluid Mech. 834, 237–270.
Xie, Z.-T., Castro, I.P., 2008. Efficient generation of inflow conditions for large eddy simulation of street-scale flows. Flow Turbul. Combust. 81 (3), 449–470.
Yu, M., Xu, C.-X., Pirozzoli, S., 2019. Genuine compressibility effects in wall-bounded turbulence. Phys. Rev. Fluids 4 (12), 123402.
Zhou, J., Adrian, R.J., Balachandar, S., Kendall, T.M., 1999. Mechanisms for generating coherent packets of hairpin vortices in channel flow. J. Fluid Mech. 387, 353–396.